Instability Patterns of Evaporative Dendrimer Deposits

A DISSERTATION
SUBMITTED TO THE FACULTY OF THE GRADUATE SCHOOL
OF THE UNIVERSITY OF MINNESOTA
BY

Narina Jung

IN PARTIAL FULFILLMENT OF THE REQUIREMENTS
FOR THE DEGREE OF
DOCTOR OF PHILOSOPHY

Perry H. Leo, Advisor

August 2012

Acknowledgments

The project would have been impossible without supports of many people. I would like to thank my advisor Professor Leo for his continuous guidance and patience during my Ph.D study. I thank my committee members, Professor Elliott, Professor Mahesh, and Professor Cockburn for their encouraging comments. I have also got supportive helps from Donna in the main office. The passions of the graduate students at Aerospace Engineering and Mechanics have inspired me: Thanks, GV, Shankar, Hyunchul, Nikhil, Vivek, Subrahmanyam, and Susmita. My friends have encouraged me all the time: Thanks, Soyoung, Hyejung, Suyoun, Haeyoung, and those who I have met in Minnesota. I had pleasing and enjoyable times in Minnesota. Minneapolis Institute of Art was a fine place for refreshment whenever I was weary.

There was a moment when I felt like I was misplaced as a woman in the Engineering field. I would like to gratefully acknowledge Linda for her wise advice to help me find a balance in the new situations. The study abroad made me realize the real values of my family. I owe special gratitude to my family for their steadfast supports and encouragements during the project. Finally, my sincere thanks go to my husband Pilwon for his everlasting love and friendship.

This thesis is dedicated to the memory of my father

Gisik Jung

who passed away during my study.

Abstract

The purpose of this project is to understand the instability mechanism behind dendrimer pattern formation in evaporating micro-meter size droplets. Evaporation of droplets of alcohol-dendrimer solution leaves a unique solute pattern on a substrate, where the detailed structure depends on the system variables. We are interested in developing a theory of the morphology of the dendrimer deposits that encompasses evaporation effects, solvent hydrodynamics, and solute particle chemistry.

Our approach is to consider a two-dimensional coarse-grained model of dendrimer particle deposition that involves two mechanisms: transfer of solute particles by a convective flow and an inter-particle attraction competing with the convective flow. The configuration of a drying droplet is determined by the distribution of particles on a substrate and the volume fraction of them in a droplet. The Hamiltonian of each configuration is defined to account for both a convective flow and an inter-particle attraction. The evolution of the Hamiltonian is computed by Monte Carlo method to simulate the dendrimer pattern formation and associate patterns with system parameters. We found four basic regimes of morphologies that range from ringlike, wavelike, and fingerlike to islandlike patterns depending on the number of particles and the relative strength of a convective flow and an interaction.

Table of Contents

List of Tables

List of Figures

Chapter 1

Introduction

1.1 General

Recently the behavior of particles in an evaporating small droplet (μm) was explored by scanning probe microscopy (SPM) technique [5]. The experiments, reviewed in Chapter 3, found unique instability patterns that depend on experimental conditions such as the macromolecule/nanoparticle concentration and outer shell chemistry, the solvent type and evaporation rate, the surface chemistry and morphology of the substrate material, as well as the temperature of the system.

Unique morphologies - periodically 'scalloped' and molecularly stratified rings - were found by dryings a micro-meter droplet with a nanoscale dendrimer solute molecules in pentanol and hexanol solvent on mica. The detailed strucutres, stratifications, are ascribed to the effect of dendrimer surface chemistry. However, the scalloped structure imposed upon the ring structure of evporative dendrimer deposits has not been well interpreted [5, 6]. The mechanism behind the formation of scalloped rings is known partly through

the theory of solute transfer by Deegan et al [7, 8]. The theory successfully interpreted the coffee ring phenomenon that is a dark ring of coffee left behind when a coffee droplet dries on a countertop. A simple ring is formed because the evaporation induced convective flow carries the particles toward the pinned contact line.

More braodly, evaporative self-assembly of solute particles has been widely used as a simple and inexpensive way to create patterns on a solid surface [1]. Self-assembly of nanoparticles in evaporating systems is one convenient tool to make structures for a variety of applications: microelectronics or optoelectronics sensors, information processiong and data storage devices, polymer films and coatings, DNA/RNA microarrays, gene mappings, and drug discovery [1, 2, 3]. In general, the forces involved in self-assembled aggregation are weaker than ionic or covalent forces making the process reversible, but strong enough to build complex structures. The weak interaction enables particles to adjust themselves into an equilibrium structure (i.e., particles are self-assembling) [4].

1.2 Goals

This project aims to understand mechanisms for the formation of the 'scalloped' or wavelike structures left behind in a micro-meter droplet and to interpret them in terms of the competition between a convective flow and an interparticle interaction. A simple coarse grained lattice is considered to model both a convective flow and an interaction. The behavior of particles on the lattice is simulated by Monte Carlo method.

The coarse grained lattice model was proposed by Rabani et al. and is

suitable to study the effects of interactions between particles, liquid, and a substrate [9]. The model by Rabani et al. successfully incorporates with the dynamics of an evaporating thin film and diffusion of nanoparticles to describe a number of nanoparticle-self assembly patterns. It includes disk-like and ribbon-like patterns that are reminiscent of spinodal decomposition, network-like and wormlike patterns arises from nucleation and growth during evaporation of thin films [9]. Lattice models have been extended to capture a variety of structures of drying thin films including instability branched patterns [10], ringlike patterns from thin film dewetting [11], 3D stalagmites patterns in an evaporating thin film [12], structures on a diblock copolymer substrate [13], molecular pumps [14], and nanorods [15]. In most investigations using the lattice model, it is assumed that the effects of hydrodynamic convection and height change of liquid are negligible. However, describing scalloped (wavelike) pattern formation requires accounting for hydrodynamic convection for particle transport and the height change of a liquid droplet for particle deposition. The current project aims to explore the behavior of the model that includes both the hydrodynamic convection and the height change of a liquid droplet as well as inter-particle interactions.

1.3 Outline

In Chapter 2, we review general behavior of liquid thin films and sessile droplets in evaporation and the corresponding deposited patterns. The morphological 'rim' instability occurring in dewetting thin films is briefly mentioned. In Chapter 3, unique dendrimer patterns from experiments by Li et al. are presented. These experiments motivated the presesnt study. We build a coarse

grained model in Chapter 4. The simulated patterns and the comparison with the patterns obtained from the experiments are presented in Chapter 5. In Chapter 6 we discuss the results and present some ideas for future work.

Chapter 2

Literature Review

2.1 Evaporations of Liquid on a Solid Surface

Evaporation is a phase transition occurring at the liquid-air interface. Evaporation of liquid on a substrate involves several important features such as the dynamics of the droplet contact line [16], the interfacial Marangoni flow [17, 3] and the capillary flow [7]. Molecules in the liquid are carried by the evaporation-induced flows.

In this section, the evaporation of droplets and thin films are studied. The basic difference between these two classical systems is that liquid of a droplet partially wets the substrate with a finite contact angle θ_c, while a thin film completely wets the surface [18]. Evaporations in a droplet and in a film are quite different and give rise to different deposit patterns. In the following subsections we will analyze the evaporation process of each system.

2.1.1 Evaporation of Droplets

We are interested in small sessile droplets and their evaporation. First, let us consider how to determine the equilibrium shape of an axisymmetric drop on a substrate given with a liquid volume V_0. We assume that the droplet partially wets the substrate with the contact angle θ_0. Note that the rim of the droplet is where the three phases meet. We can compute the contact angle θ_0 from Young's Equation

$$\gamma_{SV} = \gamma_{SL} + \gamma_{LV} \cos\theta_0, \tag{2.1}$$

where γ_{SV}, γ_{SL}, and γ_{LV} are free surface energies between solid-vapor, solid-liquid and liquid-vapor, respectively.

The droplet shape $z = h(r, \theta)$ varies with the radius R_0, which determines the relative contribution of gravity force and surface tension γ to the shape [18]. We describe the shape with the Laplace-Young Equation:

$$p_i - p_o = -\gamma_{LV} K, \tag{2.2}$$

where p_i is a pressure in a drop, p_o is an air pressure, and K is the sum of the two principle curvatures.

Define the capillary length κ^{-1} as

$$\kappa^{-1} = \sqrt{\gamma/\rho g}, \tag{2.3}$$

where γ is a surface tension, and ρ is a density of liquid. If $R_0 < \kappa^{-1}$, the effect of gravity on the liquid pressure p_i is negligible and therefore we can

assume that p_i is constant. In this case Eq. (2.2) becomes

$$K = (p_i - p_o)/\gamma_{LV} \equiv const < 0, \tag{2.4}$$

where the curvature K is expressed in terms of the derivatives of $z = h(r,t)$. With the boundary condition $h(R_0, \theta) \equiv 0$, it is known that the droplet takes a shape of a spherical cap:

$$h(r,t) = \sqrt{\frac{R_0^2}{\sin^2\theta_0} - r^2} - \frac{R_0}{\tan\theta_0}. \tag{2.5}$$

If $\theta \ll 1$, the shape is approximately given by

$$h(r,t) \approx \frac{R_0^2 - r^2}{2R_0}\theta_0. \tag{2.6}$$

We will use this Eq. for the droplet shape in our model in Chapter 4. It is also known that the spherical caps are stable with the the contact line and the surface perturbations [19].

The evaporation rate of a droplet is limited either by mass transfer at the interface from the liquid to the air or by mass removal of by diffusion of the vapor to the surrounding air. When the diffusion of vapor in air is rapid or there is an air convection, the evaporation rate is determined by mass transfer rate from the liquid to the air. This regime is referred as transfer-rate-limited evaporation. In this regime, the evaporation is fast and uniform over the droplet, and the concentration of the vapor in air is constant. In this case the evaporation rate is proportional to the area of the droplet ($\approx R^2$), and the evaporation rate J_s is constant. Studies of deposit patterns for transfer-rate-limited evaporation are rare [20].

The alternative case is evaporation limited by vapor diffusion to the surrounding air. This regime is called diffusion-limited evaporation. Since the diffusive mass flux is coupled with the droplet shape (as a boundary condition of the diffusion equation), the rate is not uniform over a droplet and increases near the contact line. The rate is proportional to the radius of the droplet ($\approx R^1$), and its functional form is approximated by $J_s \approx (1-(r/R)^2)^{-\lambda}$, where $\lambda = (\pi - 2\theta_c)/(2\pi - 2\theta_c)$ and θ_c is the contact angle. Most studies on deposit patters have dealt with the diffusion-limited evaporation cases.

In either regime, we assume that relaxation of the equilibrium droplet shape is fast, compared to mass flux of evaporation. Evolution of a drying droplet is considered as a quasi-static process. Thus, we assume that the contact line is pinned at $r = R_0$ and the droplet shape maintains the shape of a spherical cap with the contact angle $\theta(t)$, which is decreasing with time.

Now let us consider the hydrodynamic convection in a droplet which is induced by the diffusion-limited evaporation. During evaporation, according to Deegan and his coworkers [8], an outward *capillary* flow is developed inside the drying droplet with a contact line pinned. The outward flow replenishes the liquid at the contact line that is removed by the evaporation. They considered the diffusion-limited evaporation rate and obtained the flow field analytically. In this case, the analytical approximation of the evaporation rate is proposed as [8]:

$$J_s(r,t) = J_0 f(\lambda)[1-(r/R_0)^2]^{\lambda}, \tag{2.7}$$

where $\lambda = (\pi - 2\theta_c)/(2\pi - 2\theta_c)$, and $\theta_c = \theta_c(t)$ is a contact angle and R_0 is the radius of a pinned droplet. Note that, in this case, $J_s(r,t)$ is strongly enhanced toward the edge of the droplet. The flow is responsible for the

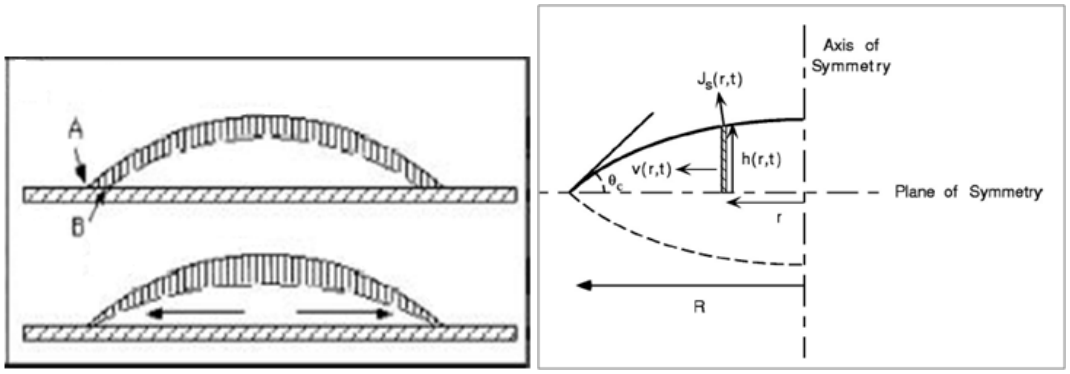

(a) Pinned contact line

(b) Evaporation rate $J_s(r,t)$ and convective flow $v(r,t)$

Figure 2.1: Shows the development of an outward capillary flow $v(r,t)$ due to the pinned contact line at the point A and the diffusion-limited evaporation rate $J_s(r,t)$ [8].

transfer of the solute particles to the contact line and for the formation of the ring-like deposits. We will study this phenomena in Chapter 2.2.1.

With the given rate $J_s(r,t)$, the equation for the height-averaged velocity field is obtained as

$$v(r,t) = -\frac{1}{\rho r h(r,t)} \int_0^r dr r \Big(J_s(r,t)\sqrt{1+(\partial_r h(r,t))^2} + \rho \partial_t h(r,t) \Big), \qquad (2.8)$$

considering the local mass balance of the liquid. Here ρ is the density of the liquid [8]. Figure 2.1 depicts development of the capillary flow due to the pinned contact line and non-uniform evaporation. We are going to use this formula to build up the Hamiltonian of particles in a drying droplet in Chapter 4.

2.1.2 Evaporation of Thin Films

Evaporation of thin films are more complicated than that of droplets, as the interaction with the substrate through van der Waals forces and electrostatic

forces is engaged [21]. When the characteristic size of a thin film reduces to sub-mirometers, thin films are not stable under the thermal height fluctuation due to these extra interaction forces [22, 23].

Consider a critical thickness of the thin film which it is unstable with respect to surface perturbation. The free energy change of the film due to surface perturbation is

$$\Delta H = \gamma \Delta A + \Delta G(h), \tag{2.9}$$

where h is the film height, ΔA is an extra area, γ is the surface energy, and ΔG is the extra interaction energy[23]. In this case, the critical wave length is computed as

$$\lambda_c = \sqrt{\frac{-2\pi^2\gamma}{d^2G/dh^2}}. \tag{2.10}$$

Note when there is no extra intermolecular energy, $G \equiv 0$, the critical wave length is infinite, resulting in the stable flat thin film. In particular, the extra interaction energy by van der Waals forces is given as

$$G = -\frac{A_{12}}{12\pi h^2}, \tag{2.11}$$

where A_{12} is the Hamaker constants. The undulation of the free surface of the thin film with a certain wave length λ increases the surface energy but the total energy decreases due to the van der Waals forces. The competition between the two energies determines the critical height h_c [22].

The dewetting behaviors of thin films depend on the film thicknesses. When the thickness of the film h is large ($h > 100$ Å), the nucleation of holes are observed in the early stage of dewetting while, when the thickness decreases, the growth of uniformly distributed surface undulations are as shown

in [24](“spinodal dewetting”).

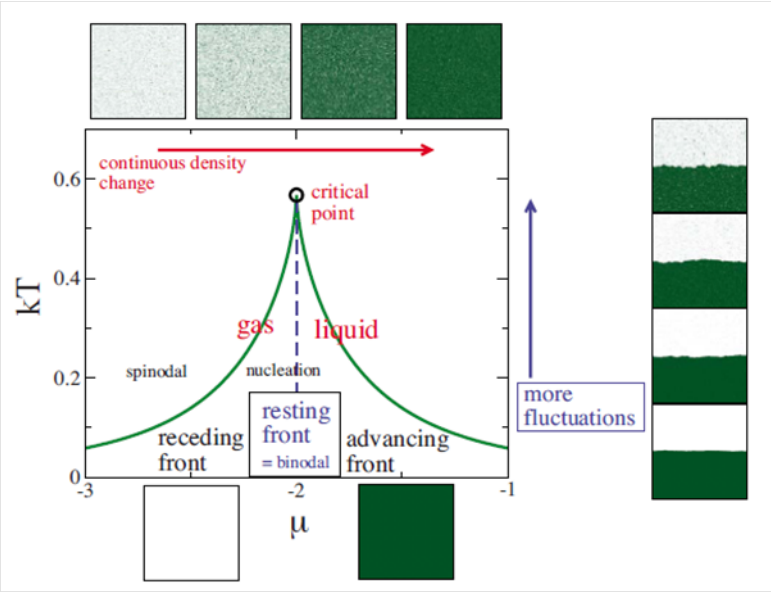

Figure 2.2: Phase diagram of a liquid thin film [10].

Now consider evaporation of a liquid thin film. The liquid-gas phase transition has been simulated by a two dimensional coarse grained Ising-type model, of the type used to describe the order-disorder transition in a ferromagnetic system [10]. The Hamiltonian of the classical Ising model is

$$E = -H \sum_i s_i - J \sum_{<i,j>} s_i s_j, \tag{2.12}$$

where $s = \pm 1$ is the spin of a cell, J is the magnetic moment, and H is the external magnetic field. If $J > 0$, the energy favors to have neighbors of the same type. Similiarly, the Hamiltonian for evaporation of a thin film, modeled by the Ising model, is

$$E = -\epsilon_l \sum_{<i,j>} l_i l_j - \mu \sum_i l_i, \tag{2.13}$$

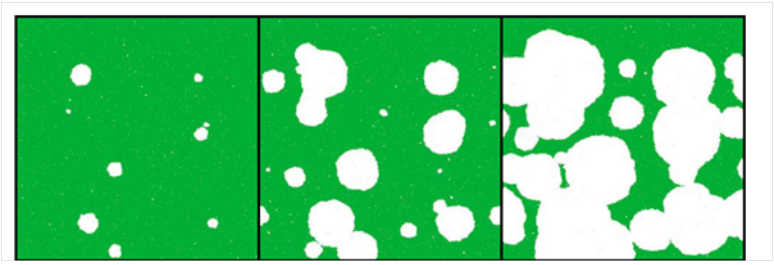

(a) Nucleation and growth of holes when $\mu = -2.3$

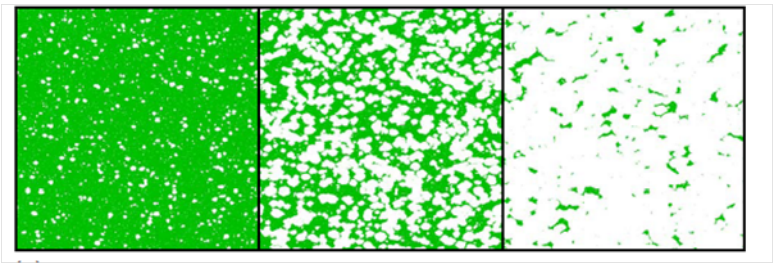

(b) Many very small holes at once when $\mu = -2.55$

Figure 2.3: Typical examples of evaporation of liquid thin films

where l_i is the state of a cell i – liquid ($l_i = 1$) and gas ($l_i = 0$), ϵ_l is the interaction energies for the nearest sites filled with liquid, and μ is the chemical potential that drives the evaporation of liquid to gas. The critical chemical potential $\mu_c = -2$ and the measure of temperature $kT_c \approx 0.567$ are computed in the system [10].

Figure 2.2 shows the equilibrium phases and the resulting behavior of evaporation of a thin film. The evaporation dynamics follows either a nucleation and growth process or a spinodal-like process depending on the chemical potential μ at a given temperature [10]. At the critical point $\mu_c = -2$, liquid and gas coexist. Where μ is close to $\mu_c = -2$, nucleation and growth of holes occur (See Fig. 2.3(a)). At the larger value of $|\mu|$, very small holes of gas are created at once (See Fig. 2.3(b)). These two limits of evaporation are responsible for the various self-assembled nanoparticle patterns on substrate [9, 10] and reviewed in Chapter 2.2.2.

2.2 Evaporative Deposit Patterns

2.2.1 Coffee Ring Deposits

The formation of coffee rings is a manifestation of the effect of the convective capillary flow in the droplet [7]. Figure 2.4 shows one of examples of ring-like deposits left after evaporation [25]. In the model for particle transport developed by Deegan et al. [8], particles are assumed to be carried by the capillary flow $v(r,t)$ until they deposit near the contact line. That is, the dynamics of the droplet are not affected by the particles. We will assume the same in our model for wavelike deposits in Chapter 4.

Figure 2.4: Light microscopy image of a ring formed by slow evaporation of a drop of an aqueous suspension containing 60 nm nanospheres on mirror quality titanium disk. Deviation from circularity indicates nonuniform contamination of the titanium surface. Ring diameter is 4.2 mm. See reference [25].

The morphological features of ring-like deposits depend on the types of the evaporation rate J_s [8]. Three different evaporation regimes are considered in Deegan's experiments: diffusion-limited evaporation where J_s is enhanced toward the contact line, transfer rate limited evaporation where J_s is constant over a droplet, and evaporation in a chamber which is artificially set up to

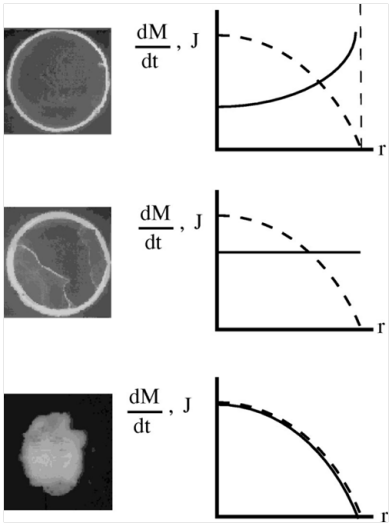

Figure 2.5: Photographs of the resulting deposit left by three identical drops dried under different conditions are shown in the left column [8].)

compare with the experimental results from the previous two. In the last case the droplet is evaporated in the chamber with a small hole above the center of the droplet so that J_s is largest at the center and goes to zero at the contact line. That is, the profile of the evaporation rate is similar to the shape of the droplet. Figure 2.5 illustrates the schematic profile of the three types of evaporations in the right column and the corresponding deposit patterns in the left column. The first two rows show ring-like patterns with different widths. The enhanced evaporation rate near the contact line in the first case creates a thinner ring than that from the constant evaporation rate. There is no ring-like pattern for the third case since no capillary flow is developed. In the simulation presented in Chapter 5, we consider diffusion limited evaporation to generate the ring-like patterns.

2.2.2 Self-assembly of Nanoparticles

Self-assembly of nanoparticles is a convenient technique to make nanostructures [26]. Unit particles or building blocks are induced to self assemble into a desired structure. This bottom-up approach involves very little manipulation of each unit particles. Other methods such as scanning probe or nanoscale nanolithograpy techniques control each molecules to construct nanostrcutres. This is generally very slow and expensive [26]. Self-assembly of nanoparticles is a spontaneous response of particles to find the lowest energy level under thermodynamic constraints and conditions (usually specified as 'static' self-assembly [4]). The applications of self-assembled structures covers electronic or optical devices, monolayered or multi-layered structures, and nanostructure arrays. In general, the forces involved in self-assembled aggregation are weaker than ionic or covalent forces which make the process reversible, but strong enough to self-fabricate complex structures.

In this section we focus on the self-assembly process occurring during the evaporation of a thin film. Nanoparticles rearrange and make various patterns due to the dynamics of the evaporation. Studies show the way to control and to tune self-assembly process using mixtures of two types of nanoparticles[25], nanorods[15], and patterned substrate [27, 28]. Two and three dimensional models are developed for monolayered[9] and multilayered structures[28, 12], respectively. Simulations of systems out of equilibrium often provide insight into the kinetics of the evaporation and the self assembling processes.

Rabani and his coworkers [9] first proposed non-equilibrium models that include the kinetics of evaporation in the pattern forming process.

A mesoscopic coarse grained lattice model is used for the self-assembly

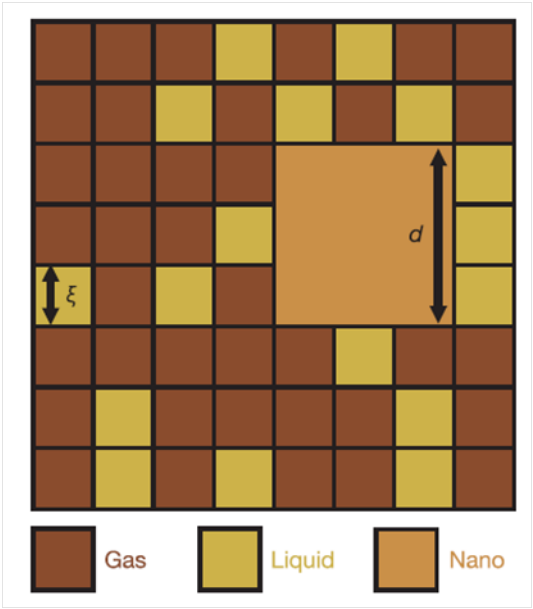

Figure 2.6: A sketch of the square lattice and important length scales of the mesoscopic model [9]. Here η is the size of the solvent's correlation length and d is the size of a nanoparticle. It is claimed that the size of particles does not affect the qualitative results.

process of nanoparticles during the evaporation of a thin film. Figure 2.6 shows a 2D square lattice of the model. The Hamiltonian H of the system over the rectangular lattice is given by

$$H = -\epsilon_l \sum_{<ij>} l_i l_j - \epsilon_n \sum_{<ij>} n_i n_j - \epsilon_{nl} \sum_{<ij>} n_i l_j - \mu \sum_i l_i, \tag{2.14}$$

where l_i (=0 or 1) is a binary variable for liquid, n_i (=0 or 1) is a binary variable for a particle at i, ϵ_l, ϵ_n, and ϵ_{nl} are interaction energies between cells of liquid and liquid, particle and particle, and particle and liquid, respectively. Also μ is the chemical potential, and the first three terms only include sums on the nearest neighbor.

The value of the chemical potential μ (or similarly kT) is a control parameter to change the morphology of nanoparticles. That is, the kinetics of

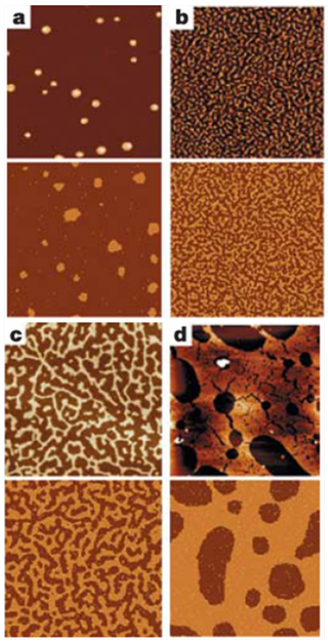

(a) Morphologies when evaporation is homogeneous in space [9]. The coverages are 5%, 30%, 40%, and 60%, respectively, for the cases *a*, *b*, *c*, and *d*.

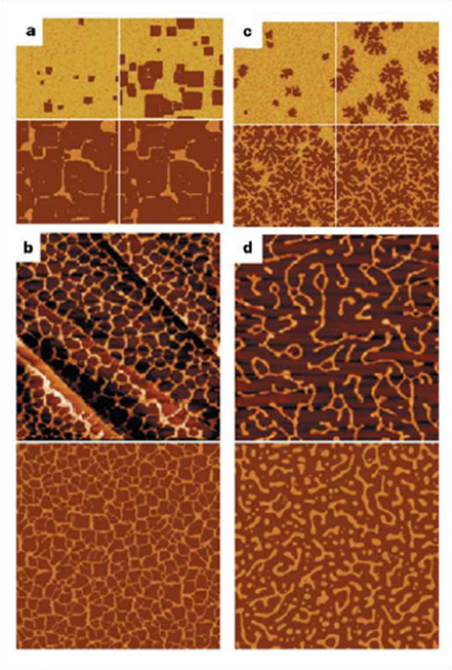

(b) Morphologies when evaporation is heterogeneous in space [9]. The coverages are 10%, 20%, 30%, and 20%, respectively, for the cases *a*, *b*, *c*, and *d*. In the case *d*, it is required that the nanoparticle domains are surrounded by solvent (i.e., the boundaries of domains are wet) through out the simulation.

Figure 2.7: Self-assembled morphologies from evaporation in experiments (top for each case) and in simulations (bottom for each case).

evaporation can alter the patterns significantly [9]. Depending on the evaporation conditions of thin films (See Fig. 2.3), two distinct mechanisms of self-assembly process are found. When evaporation is homogeneous (See Fig. 2.3(b)), it shows a simple coarsening behavior that is similar to ferromagnetic phase ordering and spinodal decompostion. The corresponding patterns are disk-like when the coverage is low while they are ribbon-like (percolating through the lattice) when the coverage is high (See Fig. 2.7(a)). On the other hand, when evaporation is strongly heterogeneous in space (See Fig. 2.3(a)),

the phase change occurs through nucleation and growth of vapor bubbles. The corresponding patterns are either network-like or worm-like domains (See Fig. 2.7(b)).

The dynamics of the lattice model are simulated using the Monte Carlo dynamics with a Metropolis probability:

$$p_{acc} = min[1, \exp(\Delta H/k_B T)], \tag{2.15}$$

where k_B is Boltzmann's constant, and ΔH is the change in energy between two configurations. The evolution is stochastic (probabilistic) in solvent fluctuation and also in nanoparticle diffusion. The random walks of nanoparticles are accepted with the probability p_{acc} but only if the cell into which is a liquid, limiting phase separation of nanoparticles without solvent.

Our goal in Chapter 4 is to extend Rabani's model to capture 3D morphology of deposits of an evaporating droplet, including the effect of a convective flow.

2.3 Morphological Instability

2.3.1 Rim Instability

The dewetting process of thin films creates different patterns depending on the film thickness [29]. Figure 2.8 shows the dewetting process of toluene solvent according to various film thickness. When the thickness h is $10nm$, the spinodal-like dewetting process appears. On the other hand, when $h = 35nm$ and $h = 185nm$, it is the hole nucleation and growth that creates rims at the edge of growing dry holes. Further, the rims at $h = 35nm$ show instability

patterns with a certain wavelength.

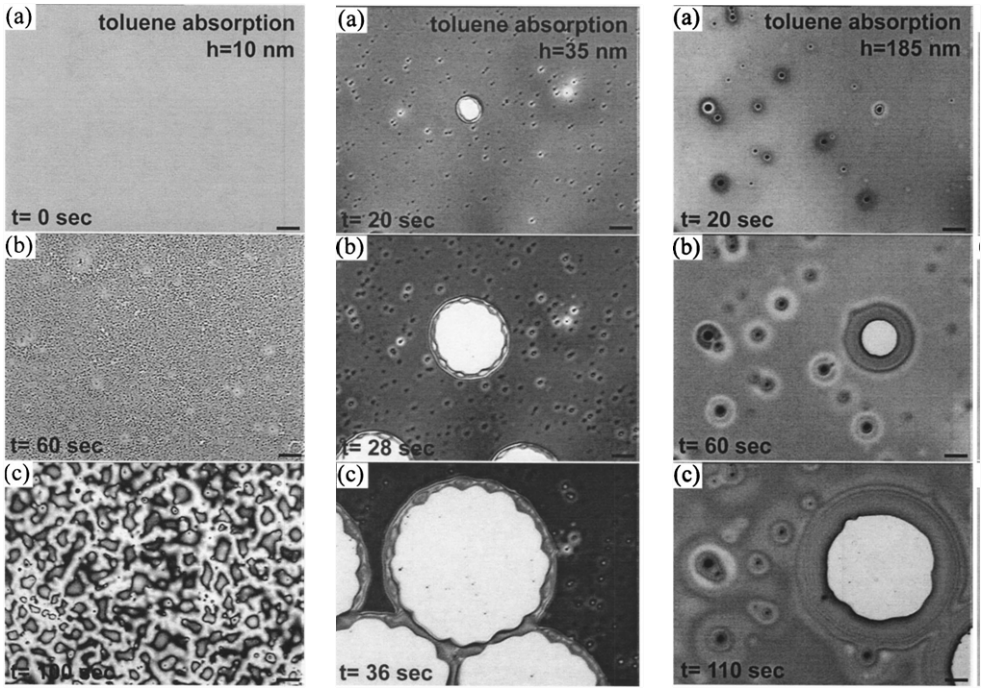

(a) The film thickness is $10nm$. It shows the time evolution of spinodal dewetting. (a) $t = 0$, (b) $t = 20$, (c) $t = 100s$. The bar scale is 100 μm.

(b) The film thickness is $35nm$. It shows the time evolution of hole nucleation dewetting. (a) $t = 20$, (b) $t = 28$, (c) $t = 48s$. The bar scale is 100 μm.

(c) The film thickness is $185nm$. It shows the time evolution of hole nucleation dewetting. (a) $t = 20$, (b) $t = 60$, (c) $t = 110s$. The bar scale is 100 μm.

Figure 2.8: Optical microscopy images of the morphologies resulting from dewetting for the film of toluene for various film thicknesses [29].

The morphological instability of dewetting rims is ascribed to reduction of the surface energy unless it is coupled to the disjoining pressure or gravity [30]. Considering the viscous flow of polymers in a perturbed rim shapes, Brochard-Wyart et al. found the critical wavelength λ_c and the fastest mode λ_m [31]:

$$\lambda_c = 2.6w; \lambda_m = 4w, \tag{2.16}$$

where w is the width of a rim. The narrow rims are more unstable than the

thick rims and break spontaneously into droplets [31].

Chapter 3

Evaporative Dendrimer Deposits: Experimental Results

In this chapter, we review the experiments by Li et al. [5, 6] on evaporative patters of monodispersed colloidal solutions of poly(aminoamine) PAMAM dendrimers. Dendrimers are three dimensional globular, highly branched macromolecules built up with a core surrounded by repeated branced units, all enclosed by a terminal surface group 'shell'. Their sizes are highly controllable ranging from one to several tens of nanometers in diameter. The layers of repeated branch units are denoted by generation numbers such as G2, G3, and G4 in the increasing order of size and density. For each generation, a definite surface group can be specified. For instance, G4 dendrimers have the primary 64 terminal amine groups and G4-50% C_{12} dendrimers have 32 primary amino surfacae groups and 32 [N (2-hydroxydodecyl)] surface groups. The surface terminal groups are closely related to the magnitudes of particle/particle or particle/substrate interactions.

In the experiments by Li et al., dilute dendrimer-alcohol solutions of 0.01wt%

or 0.005wt% were prepared. After micrometer droplets with various generations and surface groups of PAMAM dendrimers were evaporated, the resulting dendrimer deposits on a mica were imaged using atomic force microscopy (AFM) for analysis. See Fig. 3.1 for a droplet setting used in the experiment. After evaporation, unique patterns were reported that depends on the system parameters. Varying the size and the surface chemistry of the particles, evaporation rates, and concentrations, Li et al. examined unique patterns deposited after evaporation and found relations between the deposit morphology and the characteristics of the solutions.

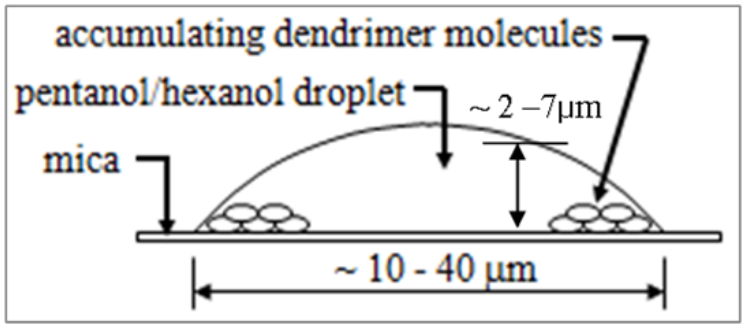

Figure 3.1: Dendrimer ring structures developed by accumulation of dendrimer molecules at the perimeter of the evaporating droplet [5].

The study shows that there are wave-like instability patterns both at small and large scales and step-like cross-sectional profiles of the deposits. These patterns are highly stratified and form periodically "scalloped" rings with the small waves at the front edges of the each stratification (See Figs. 3.2 and 3.6(b)). Together with the distinctive waves in the radial direction, there is undulation in the height of the ring, which is only ten nanometer in thickness. The characteristics of the rings are quantitatively analysed according to the diameter, d, the number of minima in the width of the ring, k, the mean wavelength of the undulation, λ, and the mean width of a dendrimer ring, w.

These were measured from the AFM images. The plot in Fig. 3.4 shows the relation between the instability wavelength λ_m and the width w of the ring-like patterns.

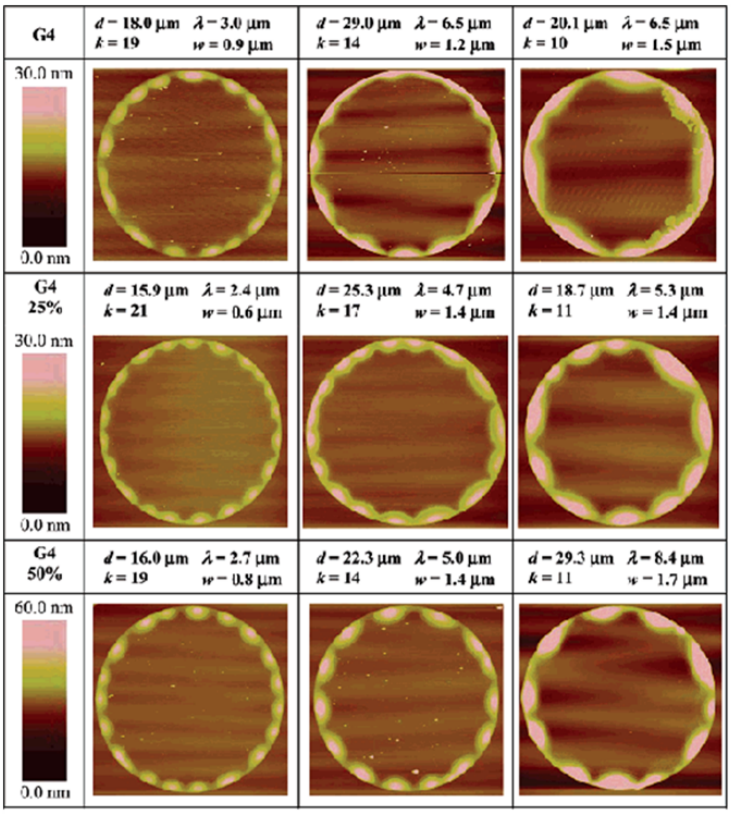

Figure 3.2: APM topgraphic images of representative ring structures fromed by evaporation of microdroplets of G4, G4-25%C_{12}, and G4-50%C_{12} dendrimer pentanol solutios of 0.05wt% on mica [5].

In one study on the effects of the surface groups on the deposit morphology, Li et al. [5] used three types of surface group: G4 ($\approx 14,000amu$ and $1.8nm$ thickness of a deposited layer, and 64 terminal amine grroups), G4$-25\%C_{12}$ ($\approx 20,000amu$ and $4.7nm$ thickness of a layer, and 48 primary amino surface groups and 16 [N-(2-hydroxydodecyl)]) and G4$-50\%C_{12}$ ($\approx 26,000amu$ and $4.7nm$ thickness of a layer, and 32 primary amino surface groups and 32 [N-(2-hydroxydodecyl)]) dendrimers in $0.05wt\%$ pentanol solutions. Refer to

Fig. 3.2. Results show that overall morphologies do not depend on particular surface group but on the mean width w of the deposit rings. Wavelength of instability is not sensitive to the surface groups but is proportional to the mean width w. The width of the rings w depends primarily on the generation numbers of particles. The width of the rings w decreases as the generation number increases for a fixed weight fraction. This is because both the density and the areal density of surface sites of particles increases with the generation number (size). The number of particles reduces with the generation number for a fixed weigth fraction. Also the packing of particles in higher generation number is more efficient since particles becomes stiffer owing to the higher areal density of surface sites. The slope of a line fitted to the data is approximately 4.6 for all particle surface groups. That is, $\lambda_m = 4.6w$ (See Fig. 3.4(a)).

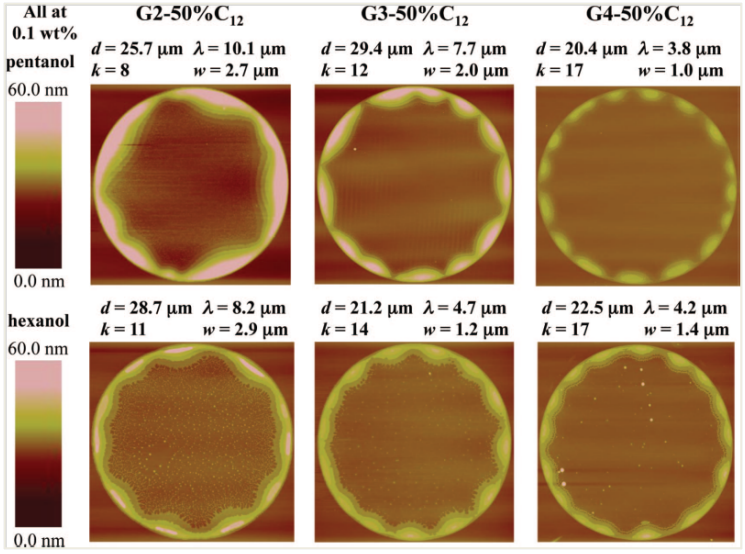

Figure 3.3: APM topgraphic images of representative ring structures formed after evaporation of microdroplets of G2-50%C_{12}, G3-50%C_{12}, and G4-50%C_{12} in both pentanol and hexanol solutions of 0.1wt% on mica [6].

A similar study using various particle sizes shows that the mean deposit width, w, also affects the overall morphology of the patterns. Three different

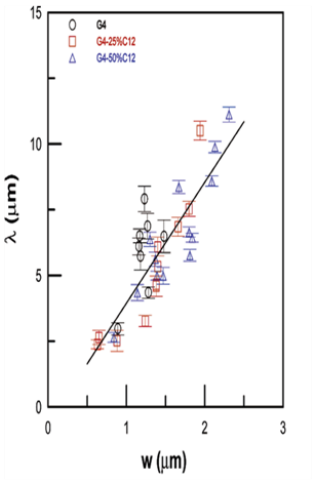

(a) Solutions are all pentanol at 0.05 wt % [5]. A line with a slope of 4.6 is drawn to indicate the tendency of the data. The error bars indicate ±1 standard deviation in the measured wavelengths [5].

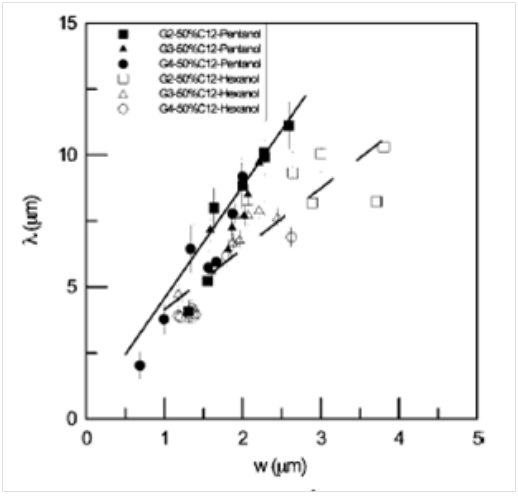

(b) The data are grouped by solvent (pentanol and hexanol). Solutions are all at 0.1 wt %. A line with a slope of 4.8 fits the trend in the data for pentanol-based solutions (solid line), whereas for hexanol a lower slope of 2.3 is estimated (dashed line). The error bars indicate ±1 standard deviation in the measured wavelengths [6].

Figure 3.4: Mean undulation wavelength, λ, vs mean ring width, w, for rings from all six dendrimer solutions.

size of dendrimers, $G2-50\%C_{12}$ ($\approx 6,000amu$ and $1.8nm$ thickness of a layer), $G3-50\%C_{12}$ ($\approx 13,000amu$ and $3.6nm$ thickness of a layer), and $G4-50\%C_{12}$ ($\approx 26,000amu$ and $4.1nm$ thickness of a layer) were used in $0.1wt\%$ pentanol solutions [6]. Refer to the top row of Fig. 3.3 for the images. One can again find a linear relation between λ_m and the width w, where the estimated ratio is $\lambda_m = 4.8w$ (See solid line in Fig 3.4(b)).

The influence of the evaporation rates are studied by comparing results from hexanol with those from pentanol solutions with the same types of the particles, PAMAM $G2-50\%C_{12}$, $G3-50\%C_{12}$, and $G4-50\%C_{12}$ dendrimers. The surface group is the same for all sizes. The evaporation rate of pentanol is three times faster than that of hexanol as calculated by vapor pressures of

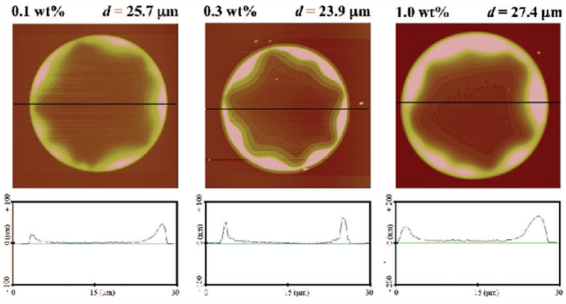

(a) Concentrations of 0.1, 0.3, and 1.0 wt %, respectively [6].

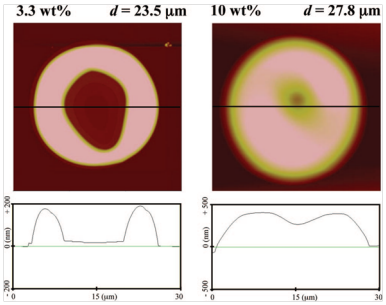

(b) Concentrations of 3.3 and 10 wt %, respectively [5].

Figure 3.5: Topographic images (30 μm × 30 μm) and radial cross-sectional scans through G2-50%C_{12}-pentanol evaporated droplets as a function of concentration.

0.488 kPa for pentanol and 0.171 kPa for hexanol, respectively at 303.15 K. In general, hexanol is heavier, denser, and more viscous than pentanol, and has less surface tension than pentanol. The contact angles made with a mica are 20° and 26°, respectively. For hexanol solutions, the instability wavelength depends on the mean width and is estimated as $\lambda_m = 2.3w$, regardless of particle sizes (See a dashed line in Fig. 3.4(b)). The slope is approximately 2.3, which is quite smaller than 4.6 or 4.8 obtained from the hexanol solutions above.

It is noted that the instability theory of a liquid rim reviewed in Section 2.3.1, predicts the fastest wavelength as $\lambda_m = 4w$. Here w is the width of the rim that is independent of material properties. It is not explained by the theory of a rim instability. Li et al. hypothesized that the significant change in slope from 4.6 or 4.8 to 2.3 may be caused by the difference in the interfacial energies between each solvent and the dendrimer deposit phase.

The patterns obtained from the solutions with different concentrations are presented in Fig. 3.5. Five different concentrations are investigated. As

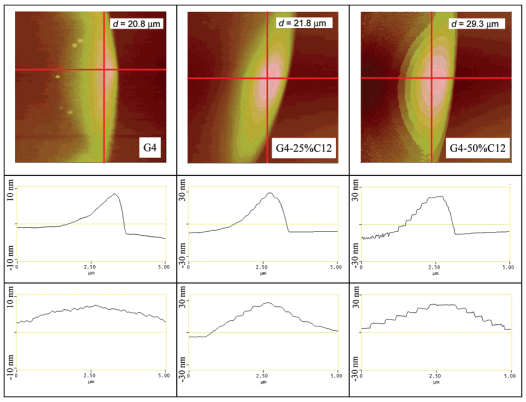

(a) Topographic images and cross-sectional scans through the representative scallop for each dendrimer molecule solution. Top row: 5μ m $\times$ 5μ m topographic images. Middle row: radial cross-sections. Bottom row: tangential cross-sections. The diameters of the rings from which they are taken are indicated [5].

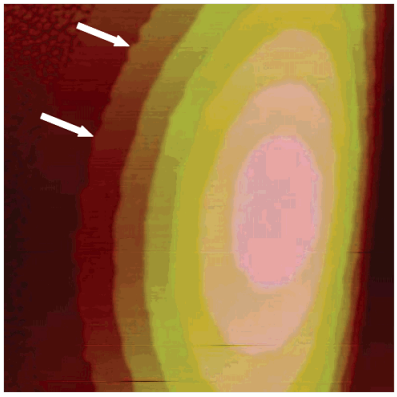

(b) Topographic images (2.5 μm $\times$ 2.5 μm) of a $G4-50\%C_{12}$ scallop illustrating the short wavelength undulation along individual terrace edges. The undulation is more pronounced at the front edge of the lower terraces [5].

Figure 3.6: The magnified topographic images scanned through a representative scallop.

the concentration increases, the wavelength as well as the thickness of the rings increase. At the higher concentrations of $3.3wt\%$ and $10wt\%$, the highly stratified and 'scalloped' rings become rather unclear.

There are also some features of deposits at nano scale. Among particles of $G4$, $G4-25\%C_{12}$, and $G4-50\%C_{12}$, those with the surface chemistry of $G4-50\%C_{12}$ make more strikingly stratified dendrimer ring structures, with a perfect dendrimer monolayer 'terraces'. The front monolayer implies small scale instability, see Fig. 3.6(b). The wavelength of these instability depends a soute type, and is shorter for pentanol solutions than for hexanol. Note that this is the reversed selection for the larger scale instability patterns shown in Figs. 3.2 and 3.3. That is, the larger λ_m for pentanol.

One of the main goals of the present work is to reveal the underlying mechanisms of wavelike deposit patterns at macro scale using a simple computational

model. This is presented in Chapter 4.

Chapter 4

A Model for Particle Depositon in a Drying Droplet

In this chapter, we introduce a coarse-grained lattice gas model to describe the deposition process of solute particles in a drying droplet. A lattice model is a simple but universal model that is used to describe properties of materials at a particle level. For example, the behaviour of gas particles is modeled with a lattice gas cellular automata. Each lattice cell in this model denotes a gas particle with a certain velocity. The Ising model is another popular lattice model to explain phase transition of magnets. Each cell carries a spin that is one of magnetic moments. The distribution of magnetic moments over the lattice defines one state of a material. Studying the equilibrium state of the lattice may predict the equilibrium properties of the material.

In our model, the substrate under a drying droplet is discretized into regular cells and the droplet is discretized into columns on the lattice. Each column carries continuous variables such as densities of the solute particles confined in the column and velocities of the particles due to solvent evaporation.

The detailed model is explained in the next three sections. In the section 4.1, we specify states of a cell and configurations of a lattice for particle redistribution. In Section 4.2, the system Hamiltonian is defined that models the physics of the solute particles during evaporation. In Section 4.3, we introduce a Monte Carlo method with a Metropolis algorithm to simulate dynamics of the system toward equilibrium deposit patterns.

4.1 A Model

4.1.1 A System and Microstates

A droplet on a solid substrate is drying at ambient conditions. The radius of the droplet is R_0 and the contact line is pinned during evaporation. The evaporation is considered as a quasi-steady state process. The droplet shape at each moment is assumed as a spherical cap $h = h(r, t)$ with the solvent of a low capillary number. The capillary number is the ratio between a viscous force and surface tension:

$$Ca = \frac{\mu V_c}{\gamma}, \tag{4.1}$$

where μ is a viscosity, V_c is the characteristic velocity scale of a system, and γ is a surface tension between a liquid and an air. At a low capillary number (generally less than 10^{-5}), flows in porous media are governed by capillary forces. In our case, the low capillary number allows to decouple the droplet shape from the convective flow field in the droplet.

We assume the solution of a droplet is initially dilute and the radius of solute particles R_M is much smaller than the droplet radius R_0 but much larger than the size of solvent particles. The solvent is considered as a continuum

medium in the model. The solute particles interact with each other through weak van der Waals forces. Solute particles get closer to each other as the solvent evaporates and the effect of particle interactions strengthen as well. We model the solute particles as hard spheres.

Let N be the total number of solute particles, which is conserved during evaporation. That is,

$$N = \sum_i N_i, \tag{4.2}$$

where N_i is the number of solute particles at a cell, i. The total energy E_{tot} of the system becomes

$$E_{tot} = \sum_i E_i, \tag{4.3}$$

where E_i is an energy at a cell, i. A configurational phase space of a drying droplet with N particles is defined by the distribution of particles $\{N_i\}$. A point in the phase space is $\nu = \{N_i\}$.

4.2 The System Hamiltonian

In the current study we consider two features related to pattern formation in a drying droplet: hydrodynamics of the solvent and weak van der Waals interactions between the solute particles. The total energy of the system in a thermal equilibrium will reflect these two mechanisms. The Hamiltonian H_ν, the total system energy with a state ν, takes the form

$$H_\nu = \sum_i f_i N_i - \sum_{<i,j>} g_{ij} N_i N_j, \tag{4.4}$$

where the first term is the contribution from the convective capillary flow of the solvent and the second term is the contribution from the van der Waals interactions of the solutes. The summation $< i, j >$ in the second term includes the sum over cells at the nearest neighbors for each cell, i. In the following subsections, the terms f_i and g_{ij} will be defined in detail.

4.2.1 Convective Flow Potential

According to Deegan's theory of particle transport [7], during diffusion-limited evaporation, an outward flow inside a droplet is developled due to the pinned contact line. The outward flow essentially carries all particles toward the contact line making ring-like patterns.

Focusing on a particle in a drying droplet, when the particle radius R_M is small compared to the radius of the droplet R_0, the motion of the particle is completely determined by the capillary flow $v(r,t)$, before it deposits near the contact line. Let F_d be the driving force of the motion of the particle. The Stokes drag law predicts the hydrodynamic force F_d on a sphere of radius R_M as

$$F_d = 6\pi\eta_m R_M v(r,t), \tag{4.5}$$

where η_m is the viscosity of the solvent and R_M is the radius of the solute molecule. The corresponding convective potential of a particle placed at r is then defined by

$$f = \int_r^{R_0} F_d dr = 6\pi\eta_m R_M \int_r^{R_0} v(r,t) dr. \tag{4.6}$$

In defining f from $v(r,t)$, two things are required: its dimensions should

be energy and its gradient should be negatively proportional to the flow $v(r,t)$ so that it shows the tendency of particles to flow along with $v(r,t)$. To derive Eq. (4.6), we first compute the work done W by the force moving a particle from r to the contact line $r = R_0$:

$$W_{|r\to R_0} = \int_r^{R_0} F_d dr.$$

Next the potential energy change Δf of a particle displaced from r to R_0 is computed as

$$\Delta f = f(R_0) - f(r) = -W_{|r\to R_0}.$$

The position $r = R_0$ is chosen as a standard reference point resulting in $f(R_0) = 0$. The potential field finally becomes

$$f(r,t) = W_{|r\to R_0} = 6\pi\eta_m R_M \int_r^{R_0} v(r,t)dr,$$

as given in Eq. (4.6). We call the potential the *convective flow potential*. By discretization of f we obtain f_i, a potential energy of a particle at a cell, i.

Before morphologies of deposits are studied, we consider the computation of the convective potential induced by the diffusion limited evaporation for the first term of the Hamiltonian in Eq. (4.4).

4.2.1.1 Computations for Convective Potentials

In this section, we compute the convective velocity field v_i for the term $\sum_i f_i N_i$ given in Eq. (4.4). The field $v(r,t)$ is computed from the given evaporation rate $J_d(r,t)$ and the change of a droplet shape $\dfrac{\partial h}{\partial t}$, where $h(r,t)$ is a spherical

cap shape. We assume the diffusion limited evaporation $J_d(r,t)$ in the following computation. The functional forms of the droplet shape $h(r,t)$ and the evaporation rate $J_d(r,t)$ are

$$h(r,t) \approx \frac{R_0^2 - r^2}{2R_0}\theta(t),$$

and

$$J_d(r,t) = \rho\omega_0(1+\lambda^2)[1-(r/R_0)^2]^{-\lambda}, \tag{4.7}$$

where we assume a small contact angle $\theta(t) \ll 1$ and

$$\lambda = \frac{\pi - 2\theta(t)}{2\pi - 2\theta(t)}. \tag{4.8}$$

The constant ω_0 which sets the evaporation rate adn has units of velocity will be determined so that the velocity field $v(r,t)$ becomes in the range of some characteristic velocity V_c, which will be chosen later in Eq. (4.11).

To specify $\dfrac{\partial h}{\partial t}$ in terms of the contact angle evolution $\theta(t)$, the mass balance of the evaporated solvent is used. We will first specify $\theta(t)$ and the final drying time t_f using the mass balance. That is, the solvent mass loss with $J_d(r,t)$ is balanced by the corresponding droplet volume change:

$$\rho\frac{\partial}{\partial t}V(t) = -\int_0^{R_0} 2\pi r\sqrt{1+(\partial_r h)^2}J_d(r,t)dr,$$

where $V(t)$ is a volume of a spherical cap shape and given as

$$V(t) = \frac{\pi R_0^3}{3}\Big(2 - 3\cos\theta(t) + \cos^3\theta(t)\Big).$$

The equation yields an ODE for the contact angle $\theta(t)$,

$$R_0\theta^3(t)\theta'(t) = -\omega_0\left(\frac{5}{2} - \frac{7\theta}{2\pi} + \frac{\theta^2}{2\pi^2} + \frac{\theta^3}{2\pi^3}\right),$$

where we use the small angle assumption $\theta(t) \ll 1$ which gives

$$\left(\frac{\partial h}{\partial r}\right)^2 \approx 0 \quad \text{and} \quad \sin^3\theta(t) \approx \theta^3(t).$$

Using an initial condition of $\theta(0) = \theta_0$, the solution $\theta(t)$ is then implicitly given as

$$\begin{aligned}\frac{\pi^3}{6}\Bigg(&12\theta - 6\pi\log(\pi-\theta) + (8\sqrt{6}-3)\pi\log\Big((\sqrt{6}-1)\pi-\theta\Big)\\ &-(8\sqrt{6}+3)\pi\log\Big((\sqrt{6}+1)\pi+\theta\Big)\Bigg) = -\frac{1}{R_0}\omega_0 t - 577.2287, \quad (4.9)\end{aligned}$$

and t_f is also computed using the fact that $\theta \equiv 0$ at the final time t_f:

$$t_f = 0.0016922 \times \frac{R_0}{\omega_0}. \quad (4.10)$$

The final drying time is proportional to the droplet size R_0 and inversely proportional to the evaporation rate ω_0. The linear dependence on R_0 agrees with the fact that the evaporation rate is linearly dependent on the droplet size in the case of the diffusion limited evaporation.

Finally, with the computed values of $J_d(r,t)$, $h(r,t)$, and $\dfrac{\partial h}{\partial t}$, we numerically obtain the convective flow field $v(r,t)$, and then compute the convective potential f_i and the Hamiltonian term $\sum_i f_i N_i$ given in Eq. (4.4).

We assume that the capillary number $Ca \ll 1$ in Eq. (4.1) is for a spherical cap and the convective capillary flow. Then, if we take at $Ca \approx 10^{-7}$ and

$\omega_0 = 0.01$,

$$V_c = \frac{\sigma Ca}{\eta_m} = \frac{\sigma}{\eta_m} 10^{-7} \approx R_0/sec, \tag{4.11}$$

where $\sigma = 25.7 dynes/cm$ is a surface tension and $\eta_m = 4cP$ is a viscosity of solvent, respectively. The order of magnitude of the computed velocity field becomes comparable with R_0 per second.

4.2.2 Van der Waals Potential

The van der Waals force, in particular the so called London dispersion force, is an intermolecular force which is relatively weak compared with covalent or ionic bonding forces. The forces are due to the induced dipoles when two neutral molecules are brought close together. Given two spheres of radius r_M separated by a distance $z \gg r_M$, their van der Waals interaction is described by the energy $\Phi_p(z)$:

$$\Phi_p(z) = -\frac{C}{z^6}, \tag{4.12}$$

where C is a constant.

In the case of two macroscopic bodies, according to Hamaker and his coworkers, the interaction energy can be approximated by summing all the pairwise interactions Φ_p in Eq. 4.12 over the volumes of the two bodies [32]. As an example, the interaction energy Φ_{bdy} between two macroscopic spheres of radius R_{bdy} separated by a distance $d \ll R_{bdy}$ is obtained by simply summing all pair interactions Φ_p and computed as

$$\Phi_{bdy}(d) = -\frac{A_{Ham}}{12} \frac{R_{bdy}}{d},$$

where the coefficient $A_{Ham} = \pi^2 C \rho_1 \rho_2$ is the Hamaker constant, ρ_1 and ρ_2 are the number densities of bodies 1 and 2, $\rho_1 = \dfrac{N_1}{V_1}$ and $\rho_2 = \dfrac{N_2}{V_2}$, respectively.

In our model, we need to compute the total number of interactions between particles in two adjacent cells, i and j. We assume that N_i-particles are uniformly distributed in the cell i and there is no particles in a space with the width of R_M at the interface of each cell to prevent the particles from contacting each other.

The total interaction energy between cells i and j is given as a double integral:

$$\int_{R_M}^{S-R_M} \int_{R_M}^{S-R_M} \frac{-C_{disp}}{(S-x+z)^6} \left(\frac{N_i}{V_i} A_{ij}\right) \left(\frac{N_j}{V_j} A_{ij}\right) dxdz,$$

where $R_M \leq x \leq S - R_M$ and $R_M \leq z \leq S - R_M$, $s = S - x + z$, and A_{ij} is the area at the interface of the volume V_i and V_j, and S is the length of a cell in the r direction. See Fig. 4.1 for variables of two adjacent cells i and j. In computing the distance between particles s, for simplification, we ignore both the height dimension of the droplet and the y-axis dimension of a cell. This is because the height is low and decreases with time and y-axis dimension is similar orders of magnitude to x-axis dimension. This simplification will only affect the constant coefficient, C_{disp}, of the total interaction energy. Let us define g_{ij} for the unit energy when $N_i = 1$ and $N_j = 1$:

$$g_{ij} = \int_{R_M}^{S-R_M} \int_{R_M}^{S-R_M} \frac{-C_{disp}}{(S-x+z)^6} \left(\frac{A_{ij}}{V_i}\right) \left(\frac{A_{ij}}{V_j}\right) dxdz \approx \frac{C_{disp}}{320} \frac{1}{R_M^4} \frac{A_{ij}^2}{V_i V_j} \quad (4.13)$$

where cells i and j are nearest neighbors.

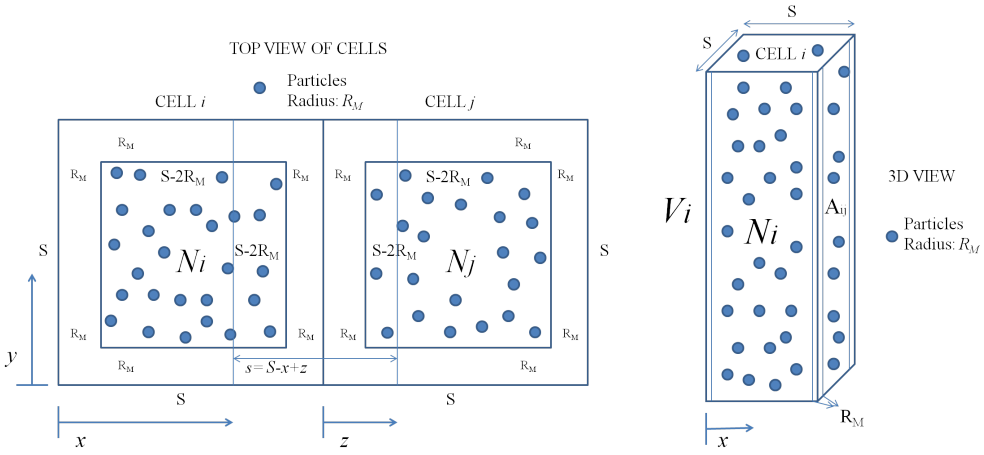

(a) Shows variables x, z, and s of cells i and j.

(b) Shows volume V_i, particle number N_i, and area A_{ij} of a cell i.

Figure 4.1: Schematic illustration for variables used in computing interaction energy at two adjacent cells i and j.

4.3 Nondimensionalization

Recall that the Hamiltonian is given as

$$H = \sum_i f_i N_i - \sum_i g_{ij} N_i N_j, \tag{4.14}$$

where f_i is an external axisymmetric potential field, N_i is the number of particles, and g_{ij} is the van der Waals interaction energy between cells i and j containing only one particle, respectively.

The convective potential field f_i is given as

$$f_i = 6\pi\eta_m R_M \int v_i dr,$$

where η_m is a viscosity of solvent and R_M is the radius of solute, v_i is a velocity

of a convective potential. The interaction g_{ij} between cells i and j is given as

$$g_{ij} = \frac{C_{disp}}{320}\frac{1}{R_M^4}\frac{A_{ij}^2}{V_i V_j},$$

where A_{ij} is the area at the interface of the two adjacent volumes V_i and V_j, and S is the cell size. The area A_{ij} is given as

$$A_{ij} = S \times h\Big(\frac{r_i + r_j}{2}, t\Big), \tag{4.15}$$

where S is the length of a cell, and r_i and r_j are the center positions of cells, i and j. The volume V_i is computed from

$$V_i(t) = \int_i h(r,t)dA_i = \int_{\theta_i}^{\theta_i+d\theta}\int_{r_i}^{r_i+dr} h(r,t)rdrd\theta, \tag{4.16}$$

where A_i is the area of a cell, i.

We introduce the following scalings to nondimensionalize the Hamiltonian. Let L, ϵL, and V_c be the characteristic scales for the length of a droplet, the length of a particle, and the velocity of the convective flow, respectively, where ϵ is the ratio of the size of solute particles to the size of a droplet and is small compare to the length scale L. The characteristic energy scale is denoted by J_0 and defined as

$$J_0 = 6\pi\eta_m\epsilon^2 L^2 V_c. \tag{4.17}$$

The upper script $*$ is for the dimensionless values.

$$R_0 = LR_0^*;\ r = Lr^*;\ R_M = \epsilon LR_M^*;\ S = \epsilon LS^*$$

$$h = \epsilon L h^*;\ v = V_c v^*;\ \int dr = \frac{1}{L}\int^* dr^*;\ A_{ij} = \epsilon^2 L^2 A^*_{ij}$$

$$H = J_0 H^*$$

The convective potential f_i scales as

$$\begin{aligned} f_i &= (6\pi\eta_m \epsilon V_c) {R^*_M}^6 \int^* v^*_i dr^* \\ &= (6\pi\eta_m \epsilon^2 L^2 V_c) f^*_i = J_0 f^*_i \end{aligned} \tag{4.18}$$

and the van der Waals potential becomes

$$g_{ij} = \left(\frac{C_{disp}}{320}\frac{1}{\epsilon^6 L^6}\right)\frac{{A^*_{ij}}^2}{{R^*_M}^4 V^*_i V^*_j} \tag{4.19}$$

$$= \left(\frac{C_{disp}}{320}\frac{1}{\epsilon^6 L^6}\right) g^*_{ij} \tag{4.20}$$

Then the Hamiltonian in Eq.(4.14) becomes

$$H = J_0 H^* = -J_0 \sum f^*_i N_i - \frac{J_0}{Q}\sum_{<i,j>} g^*_{ij} N_i N_j, \tag{4.21}$$

where Q is the dimesionless number of

$$Q = \frac{1920\pi\eta_m \epsilon^8 L^8 V_c}{C_{disp}}. \tag{4.22}$$

The scale of the term $\epsilon^8 L^8$ of a system shows that the behavior is mainly governed by the size of a system. As ϵL increases, the dimensionless number Q increases resulting in the dominance of the convective flow. When the characteristic size L is fixed, the smaller the relative size of solute particles

is, i.e., for smaller ϵ, the stronger the contribution of van der Waals forces. As an example, when $\eta_m = 0.4cP$ for pentanol, $\epsilon = 0.015$, $L = 10\mu m$, $V_c = 10\mu m/s$, and $C_{disp} = 10^{-77} J \cdot m^6 = 6.24 \times 10^{-23} eV \cdot \mu m^6$ [32], the energy scale $J_0 = 1.06 \times 10^{-3} eV$ and the dimensionless number becomes $Q = 6.15 \times 10^{17}$, which presents that the effect of the convective flow is a dominant effect for the particle transport and the deposition process. On the other hand, when $\epsilon = 0.001$, $J_0 = 4.68 \times 10^{-6} eV$ and $Q = 2.4 \times 10^8$.

The interaction constant C_{disp} contribute inversely proportionally to the dimensionless Q number. The weaker particle interaction gives the larger Q resulting in the dominance of the convective flow. The viscosity and the characteristic velocity also increase the value of Q.

The thermal energy $k_B T$ will be determined so that it is comparable with the energy scale, $k_B T \approx J_0$ during the simulation. The detailed parametric studies will be presented in the following sections 5.

The model is used to investigate the behavior of a drying droplet without and with particle interations in the next Sec.5.1. Then we will discuss a parametric study of the wave-like instability in Sec. 5.2.4.

4.4 Simulation Settings

The Hamiltonian of N-particles is computed by using the Metropolis Monte Carlo Method. Using the method, we find the configuration of particles that minimizes the Hamiltonian starting from a randomly distributed particles.

The droplet radius R_0 is divided into n_0 layers (See Fig. 4.2). Let $dr = \dfrac{R_0}{n_0}$ be the width of one layer. In the division, the number of cells in a layer is determined by keeping the area of each cell approximately $A_0 = dr^2$. Then

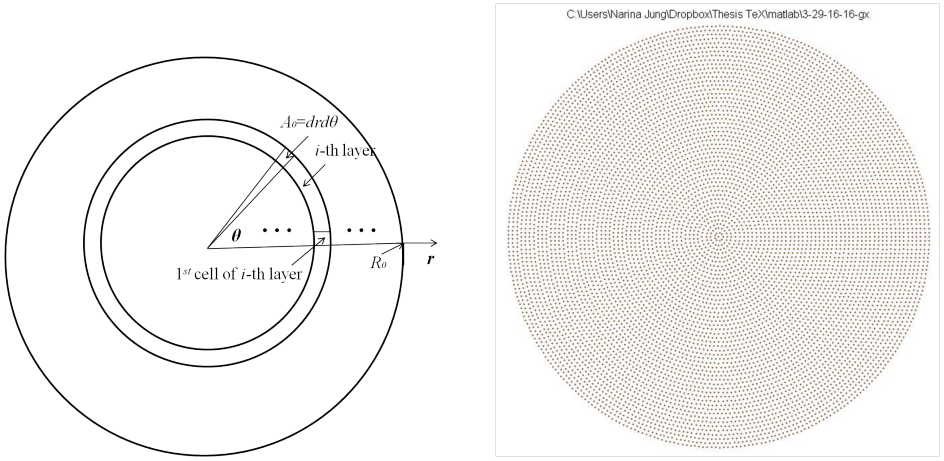

(a) Schematic illustration of the cell divisions. The droplet radius R_0 is divided into layers and each layer is divided into cells. The area of a cell A_0 is constant for all layers.

(b) Shows a full set of radial cells used in simulation. There are 50 layers in the r direction.

Figure 4.2: The radial grid system for a droplet on a solid substrate. This is the top view of the droplet.

the number of cells at a layer, i, becomes

$$\#\text{ of cells in the } k\text{-th layer} \approx \frac{A_k}{dr^2} = \pi(2k-1) \approx 3(2k-1),$$

where A_k is the area of the k-th annulus. Within the layer A_k, the cell at $\theta = 0^\circ$ is considered the first cells of the layer A_k (See Fig. 4.2(a)).

A single index i is labeled over a lattice, starting from the first cell of the first layer L_1 to the outer layers L_k in a consecutive way. Since we have different number of cells at each layer L_k, the cells are not aligned in the r-direction. We determine the nearest neighbors in the r-direction in the following way. The center point of a cell at a layer L_k is (r_c, θ_c) and used as a position of the given cell. The two nearest neighbors in the r-direction are obtained by moving the point (r_c, θ_c) in the positive direction and the negative direction

by dr. Then the positions become $(r_c + dr, \theta_c)$ and $(r_c - dr, \theta_c)$ located in the layers L_{k+1} and L_{k-1}, respectively. Based on these positions, we find the indexes i_{r+} and i_{r-} which are already labeled over the lattice. On the other hand, the positions of the nearest neighbors in the θ direction are $(r_c, \theta_c + dr)$ and $(r_c, \theta_c - dr)$, which are both located in the L_k layer. The corresponding indexes will be simply $i + 1$ and $i - 1$, if the index of the given cell is i.

A schematic drawing of the initial distribution of particles is shown in Fig. 4.3. Particles are assumed to be homogeneously distributed in the droplet so the number of particles at a cell is proportional to the height hence is the largest in the middle. The upper panel of Fig. 4.4 shows the darker color for more particles in the middle. Particles are not assigned at the center to avoid the center point in the calculation. The lower panel of Fig. 4.4 shows the cross sections of the initial distribution at the angle of $\theta = 5^\circ$ and $\theta = 50^\circ$. The values on the vertical axis are the numbers of particles assigned at cells along axes.

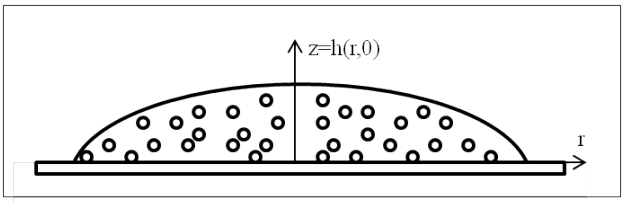

Figure 4.3: Schematic illustration of the initial distribution. It is uniformly distributed in a droplet with the proportionality to the droplet height and without exceeding the maximum volume fraction ϕ_m.

The evolution of the lattice model is stochastic (i.e., random movements of particles with given possibilities) for the transport of solute particles. The dynamics are simulated using the Monte Carlo Method. We attempt to move

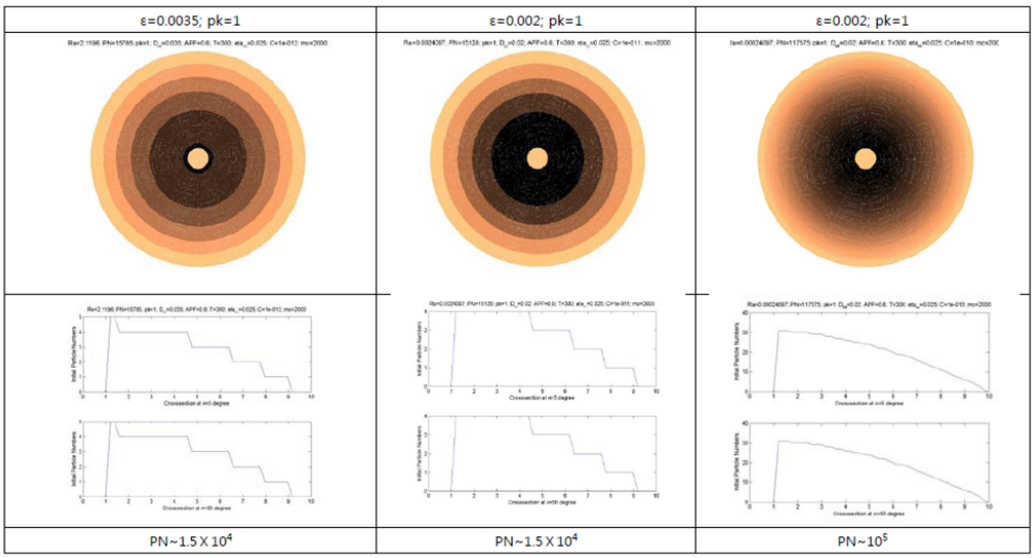

Figure 4.4: The top view of the initial distributions with the different sizes and numbers of particles.

a randomly chosen particle in a random direction, biased by the convective potential and the interaction potential defined in the previous section. Note that the dynamics conserve solute particles in a droplet and the evolution is conducted at a constant temperature T determed by the thermal energy of the system, k_BT, where k_B is Boltzmann's constant. The random attempt is accepted with the Metropolis probability,

$$p_{acc} = \exp(-\Delta H_\nu / k_B T), \tag{4.23}$$

where ΔH_ν is the resulting change in the Hamiltonian defined in (4.4).

Let N_{move} be the number of attempts per Monte Carlo step. Each step takes $\Delta\tau$ Monte Carlo seconds. The transport rate of solute particles can be controlled by changing either the value of N_{move} or $\Delta\tau$. In our model we let $N_{move} = N$ so that on average all solute particles have a chance to move per

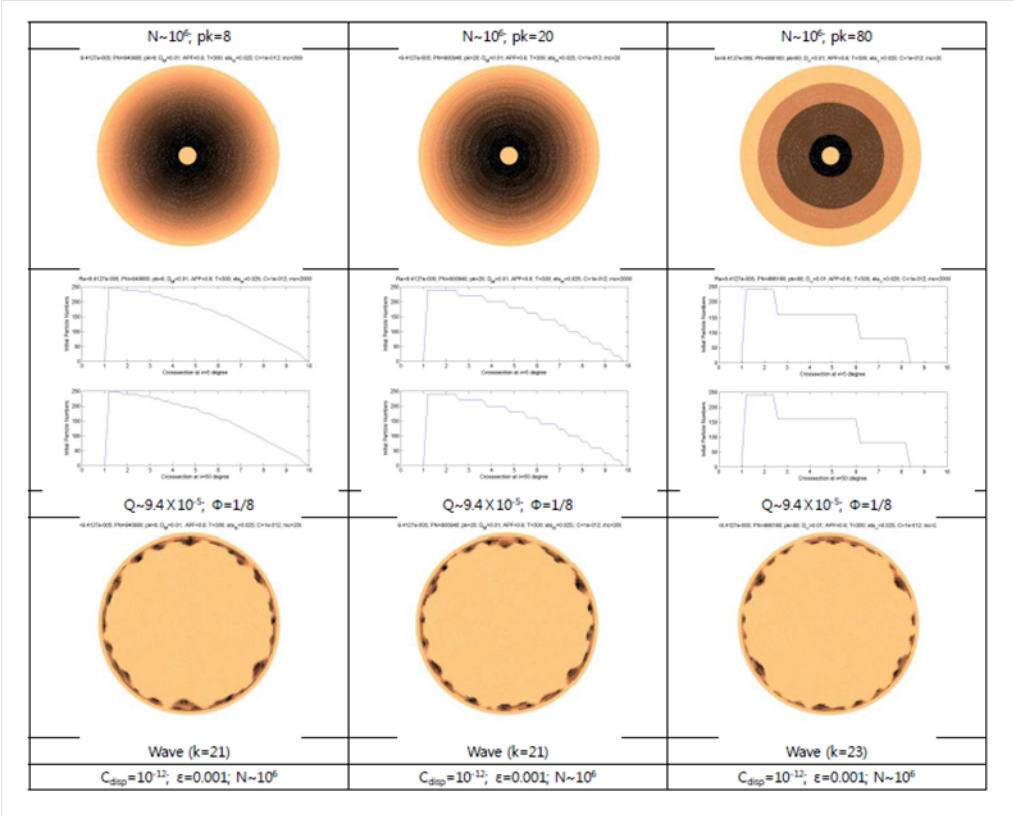

Figure 4.5: The top view of the initial distributions with the different particle unit number pk and the corresponding deposit morphology for comparison.

MC step. The value of $\Delta\tau$ is fixed resulting in a constant movement rate per step, i.e., per one evaporation cycle. When the total drying time t_f is given, the number of evaporation cycles m_c is defined as $m_c = t_f/\Delta\tau$. As $\Delta\tau$ decreases, the evaporation cycles m_c increase corresponding to the slower evaporation. The value of m_c reflects the ratio of time scales for evaporation of solvent and movements of particles.

To determine m_c, the evolution of the contact angle $\theta(t)$ is also considered. Figure 4.6 shows the numerical solution of $\theta(t)$ in Eq. (4.9) when the initial contact angle θ_0 is 0.35. The contact angle θ decrease dramatically to zero during the very short time immediately before $t = t_f$. We expect that the

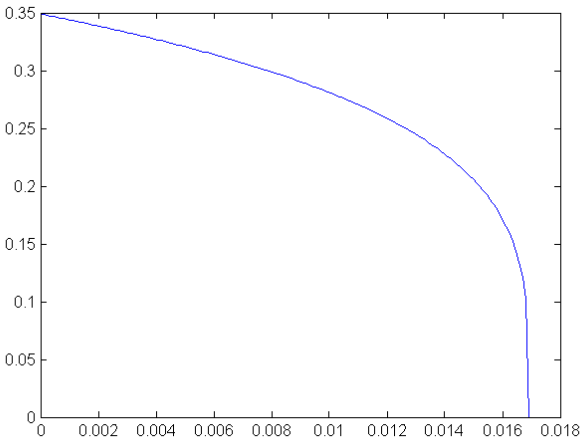

Figure 4.6: The numerical solution of $\theta = \theta(t)$ when $\theta_0 = 0.35$.

short time near t_f is important in deposit pattern formation. However, it would require very fine time scale in order to capture the behavior of a droplet and the deposition process near $t = t_f$. Instead, we assume linear decrease of the contact angle with time in our simulation:

$$\theta(t) = -\frac{\theta_0}{t_f}t + \theta_0, \tag{4.24}$$

where t_f is given in Eq. (4.10) and θ_0 is an initial contact angle.

Practically, we move multiple numbers of particles pk at the same time per trial to reduce computation time. We ensure that the value pk is small enough so that it does not affect the quality of deposit morphology. See Figure 4.5 for the relation between pk and the corresponding morphology. There is little effect of pk on morphology, though when $pk = 80$, the wave number k of the resulting instability increases slightly.

To get a deposit phase, the maximum number of particles at a cell M_i is limited by a maximum packing number ϕ_m. Since the height of a droplet h_i

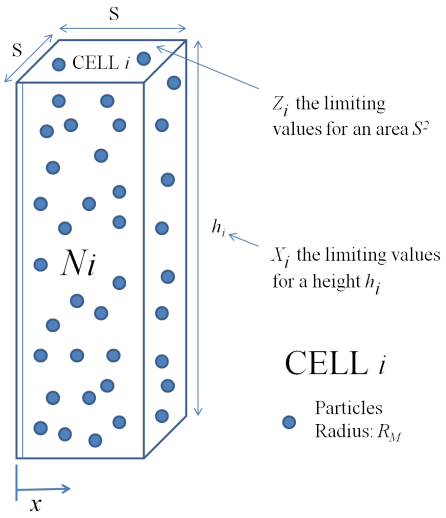

Figure 4.7: It shows variables X_i and Z_i that are limiting the maxium numbers of particles N_i for a height h_i and an cell area S^2.

reduces to zero whereas the size of cells S is constant, we limit the maxium number of particles in a cell so that the size of a particle is always less than h_i and also the total projected area of particles is always less than S^2. It is done with the maxium volume fraction ϕ_m (See Fig. 4.7) :

$$M_i = X_i \times Z_i = \phi_m \frac{S^2 h_i}{\pi R_M^3}, \tag{4.25}$$

where X_i is a length fraction

$$X_i = \phi_m^{1/3} \frac{h_i}{2R_M},$$

and Z_i is an area fraction

$$Z_i = \phi_m^{2/3} \frac{S^2}{\pi R_M^2}.$$

$$M_i = \phi_m \frac{S^2 h_i}{\pi R_M^3} \tag{4.26}$$

$$N_i < M_i \tag{4.27}$$

The movement of particles pk to a cell j with $N_j + pk > M_j$ is never accepted as the energy cost is infinite for the move. This constraint mimics the creation of the separate deposit phase at the maximum number M_j. Note that the maximum particle number M_j is a function of both N_j and V_j. That is, the evaporation rate influences the pattern forming process through the change in volume V_j of each cell. The evaporation rate can be manipulated in the simulation through $m_c = t_f/\Delta\tau$ as mentioned above. Its effect on the deposit patterns will be shown in the next Chapter.

Chapter 5

Deposit Morphologies

Deposit morphology is studied using the model for particle deposition in a drying droplet in Chapter 4. It is found that the morphology mainly depends on two dimensionless parameters: Q in Eq. (4.22) and a parameter Φ that will be defined in the following. We restate the definition of Q for reference:

$$Q = \frac{1920\pi\eta_m\epsilon^8 L^8 V_c}{C_{disp}}, \tag{5.1}$$

where η_m is viscosity of liquid, ϵL is the size of a particle, V_c is a characteristic velocity of convective flow, and C_{disp} is a constant that gives the strength of interaction. The parameter Q is the ratio of convective flow potential to interaction energy. In other words, $Q \to \infty$ means that interparticle interaction is not effective due to the strong convective flow, while $Q \approx 0$ implies that the interaction energy is dominant. Given a physical system, the value of Q plays a critical role in determining its characteristic pattern. However, we find the pattern can be altered a fixed Q using different initial numbers of particles. We introduce a new dimensionless parameter Φ to indicate the total volume

of particles. It is conveniently defined by

$$\Phi = \frac{N}{10^6} \frac{\epsilon^3 L^3}{(10^{-3} \cdot 10\mu m)^3}, \tag{5.2}$$

where N is the number of particles and ϵL is the size of a particle. The values at the denominator are chosen using the typical values of parameters in Table 5.1.

We find that patterns at fixed Q and Φ share common characteristics even when various dimensional sizes and numbers of particles and interactions are used. Figure 5.1 shows four wave patterns for fixed volume fraction $Q = 10^{-4}$ and $\Phi = 1/8$, but with different interactions, particles sizes, and particle numbers. We see that wave numbers are similar to each other (i.e., k is near 20).

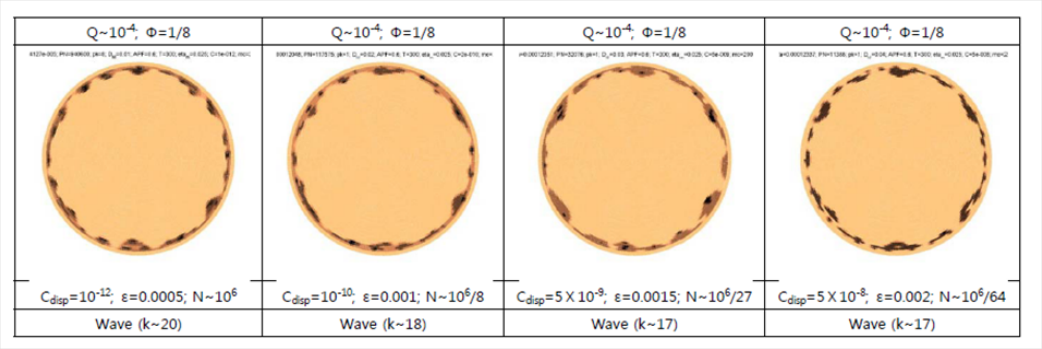

Figure 5.1: Wavelike patterns at $Q = 10^{-4}$ and $\Phi = 1/8$.

In the following section 5.1, we present an overview of the behavior of deposit patterns in terms of Q and Φ and categorize morphologies into four types. The morphology in each category will be studied in detail in the later sections. Unless otherwise stated, the values of parameters are taken from the typical values given in Table 5.1

Table 5.1: Typical Values of Parameters for Simulations

Parameters	Values
Droplet Size (R_0)	$10\mu m$
Initial Contact Angle	0.2
Particle Size (R_M)	$10nm$
Ratio Particle to Droplet Sizes (ϵ)	10^{-3}
Particle Number (N)	10^6
Temperature (T)	$300K$
Solvent Viscosity (η_m)	4.0 cP
Evaporation Rate Constant (ω_0)	0.01
Capillary Number (Ca)	10^{-7}
Maximum Volume Fraction (ϕ_m)	0.6
Monte Carlo Steps (mc)	2000
Particle Unit Number (pk)	20

5.1 Behavior of Particles during Evaporation

We begin by investigating the change of deposit morphology by varying the values of Q with fixed Φ. Figure 5.2 shows the representative patterns of the deposit according to the interaction Q. As mentioned earlier, Q can be changed independent of Φ by changing the interaction strength C_{disp}. The change of Q is done by adjusting the strength of interactions. In the figure, the dimensionless numbers of Q and Φ are shown at the top of the panels for morphological shapes and cross-sections and the corresponding values of the systems at the below.

Four different regimes of patterns are found: ringlike, wavelike, fingerlike, and islandlike patterns. As the strength of interactions increases (Q decreases), the morphology transforms from ringlike toward islandlike patterns. That is, with weak interactions, the default deposit patterns become ringlike. On the other hand, as Q decreases, patterns transform from ringlike to islandlike. The patterns that emerge between wavelike and islandlike patterns look like fingers

aligned in the radial directions.

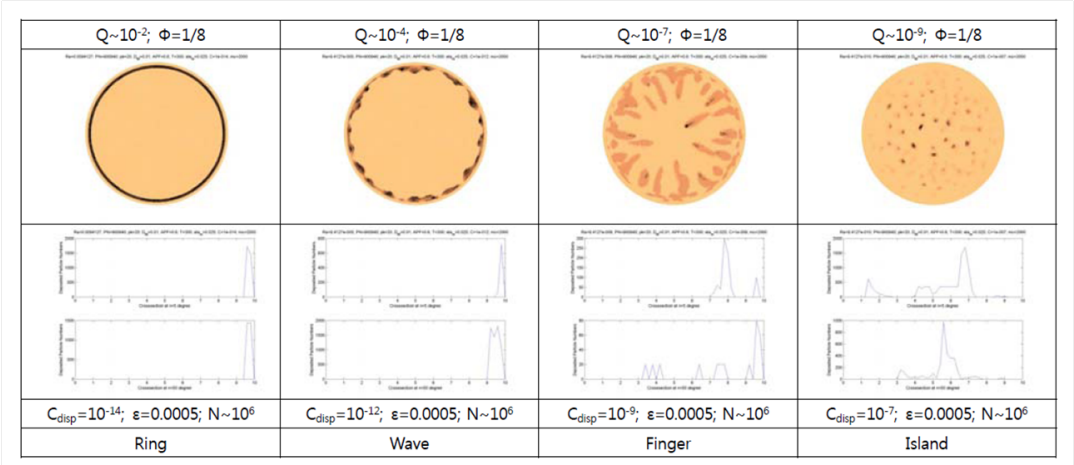

Figure 5.2: The representative patterns when $Q \approx 10^{-2}$, 10^{-4}, 10^{-7}, and 10^{-9}. We find four basic regimes of patterns: ringlike, wavelike, fingerlike, and islandlike patterns.

For the wavelike morphology, we investigate the change in wave numbers k for different values of Φ and fixed Q. The value Φ can be varied independent of Q by changing the particle number N. The patterns in Fig. 5.3 show different patterns for different Φ. The wave number k decreases as Φ increases. The mean thickness of the deposit is proportional to Φ. From left to right, Φ increases from 1/80 to 1/4 and the value Q is fixed at 10^{-4}. When $\Phi = 1/80$ the number of particles is not sufficient to create fully developed wavelike patterns.

The change of the size of particles affects not only Φ but also Q. That is, the size of particles can affect both the drag forces imposed on particles by convective flows and the total volume of particles. Figure 5.4 shows the effect on the patterns with respect to the change of ϵ. The Q values are consistent with changes in ϵ as 10^{-2}, 10^{-4}, 10^{-7}, and 10^{-9} as in Figure 5.2. One can observe as ϵ decreases that the morphology changes from ringlike to

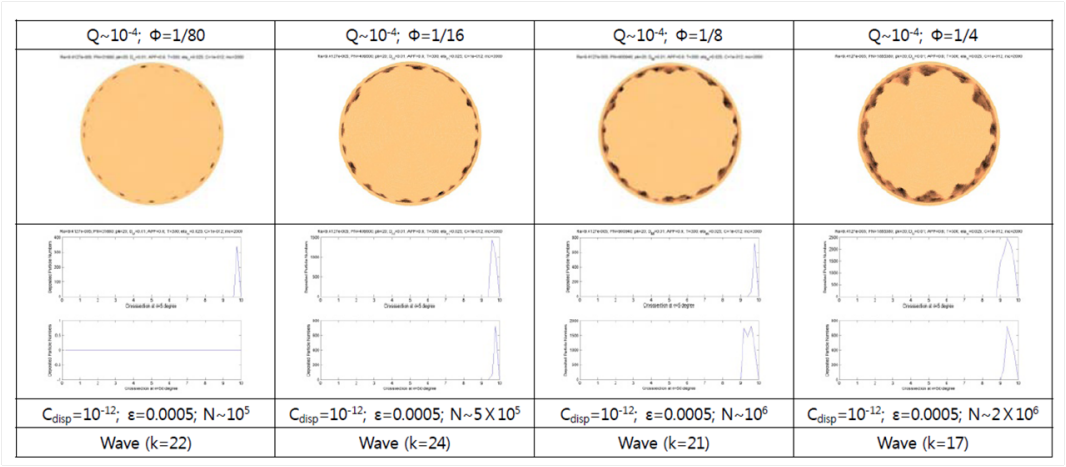

Figure 5.3: The number of particles N are varied from 10^5 to 2×10^6.

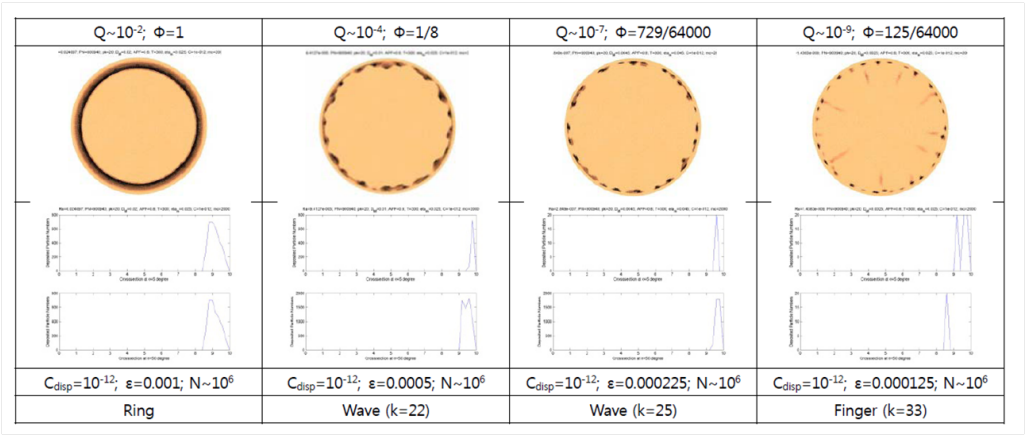

Figure 5.4: The size of particles is changed from $\epsilon = 0.000025$ to $\epsilon = 0.002$.

wavelike and to fingerlike patterns. Also, for a given value of Q, smaller Φ gives weaker interactions. For example, at $Q = 10^{-9}$, the pattern is islandlike with $\Phi = 1/8 = 125 \times 10^{-3}$ in Figure 5.2, while it is fingerlike when $\Phi = 125/64000 \approx 20 \times 10^{-3}$ in Figure 5.4.

We further investigate influence of the particle size when the volume fraction of particles Φ is fixed at $1/8$. The results are given in Figure 5.5. In order to fix Φ at the same value, the number of particles N varies from 10^6 to $10^6/42$ depending on the particle size. The tendency of morphological change from

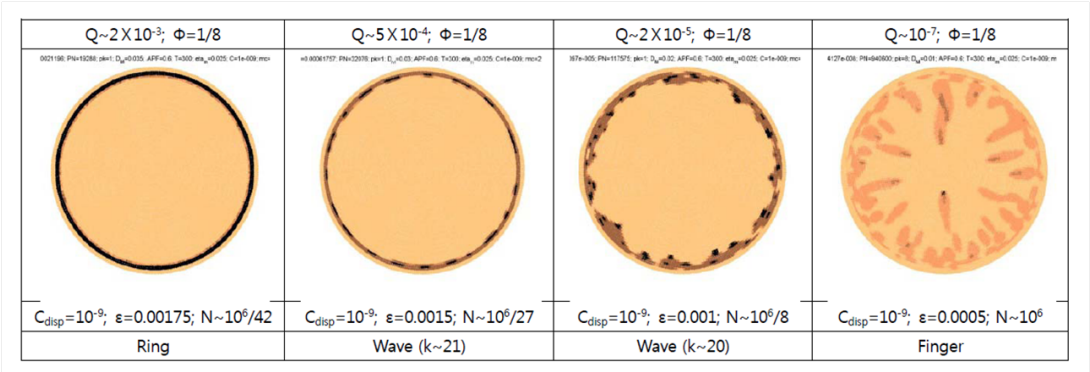

Figure 5.5: The size effects on the patterns. The volume fraction Φ is fixed. The values of ϵ used are $\epsilon = 0.0005$, 0.001, 0.0015, and 0.00175.

ringlike to wavelike to fingerlike is again seen. It is noted that Q is much more sensitive to changes in ϵ (ϵ^8 in Eq. (4.22)) than to changes in C_{disp}.

Finally, we present a spectrum of the patterns at $\Phi = 1/8$ and different Q in Fig. 5.6. The wavy shape emerges at $Q \approx 10^{-3}$ while fingerlike patterns and islandlike patterns start at $Q \approx 10^{-6}$ and at $Q \approx 10^{-9}$, respectively.

If we increase Φ larger than 1/8, the four categories of morphologies will remain the same. However, based on the studies on the effects of Q and Φ above, we can expect that islandlike patterns emerge at values of Q larger than 10^{-9} and fingerlike patterns emerge at values of Q larger than 10^{-6}. This is because when Φ increases, the average distance between particles decreases, which will also increases particle interaction.

5.2 Morphology Classification

In the previous section, four types of morphologies are identified for various values of Q and Φ: rings, waves, fingers, and islands. Each type of morphologies is now studied in more detail.

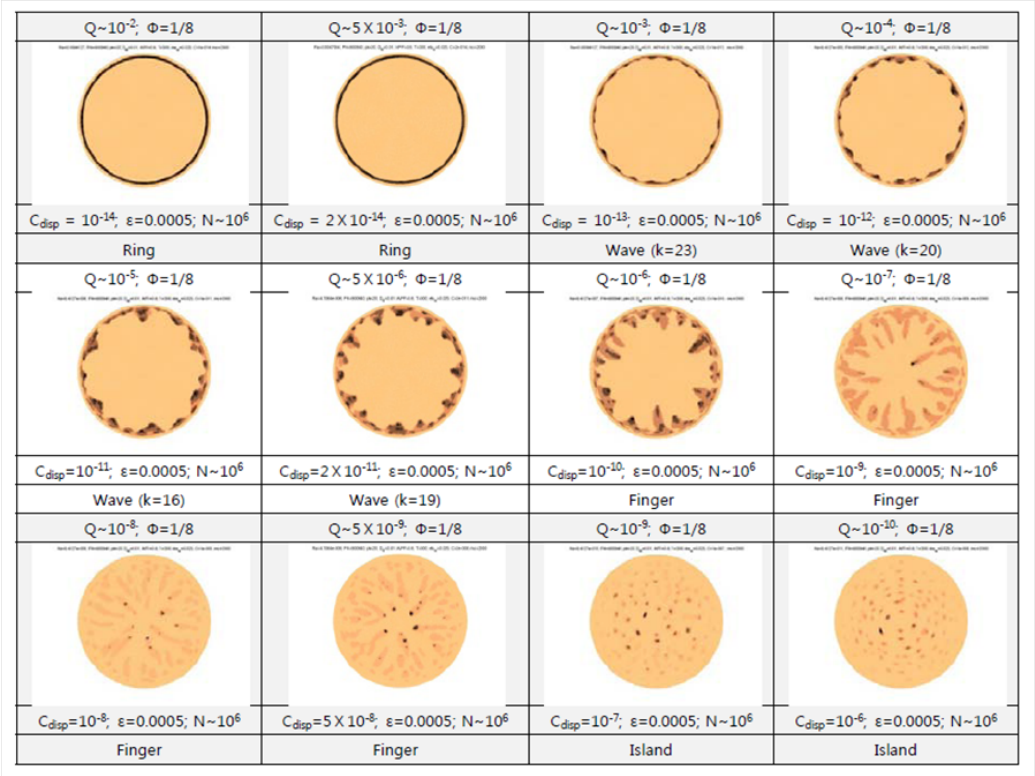

Figure 5.6: The value of C_{disp} changes from 10^{-14} to 10^{-6} $eV \cdot \mu m^6$, which correspond to the dimensionless values of Q number from 10^{-2} to 10^{-10}.

5.2.1 Ring Patterns

In the absence of particle interactions, $Q \to \infty$ in Eq. (4.14), our model of solute particle deposition is related to a simple model of the coffee-ring effect of particles. Particles that are initially uniformly distributed are transported to the pinned contact line due to a capillary driven convective flow, making a coffee ring structure. As disccused in Fig. 2.5 in Chapter 2.2.1, the morphological features of coffee-ring effect such as the width of a ring can be controlled by the convective flow $v(r,t)$ to the contact line through the evaporation rate $J_s(r,t)$. The model developed in Chapter 4 enables us to convert the given $J_s(r,t)$ to the hydrodynamic potential f_i (See Eqs. (2.8) and (4.6)).

In this study, we start by showing a typical evaporative deposits for $Q \to \infty$

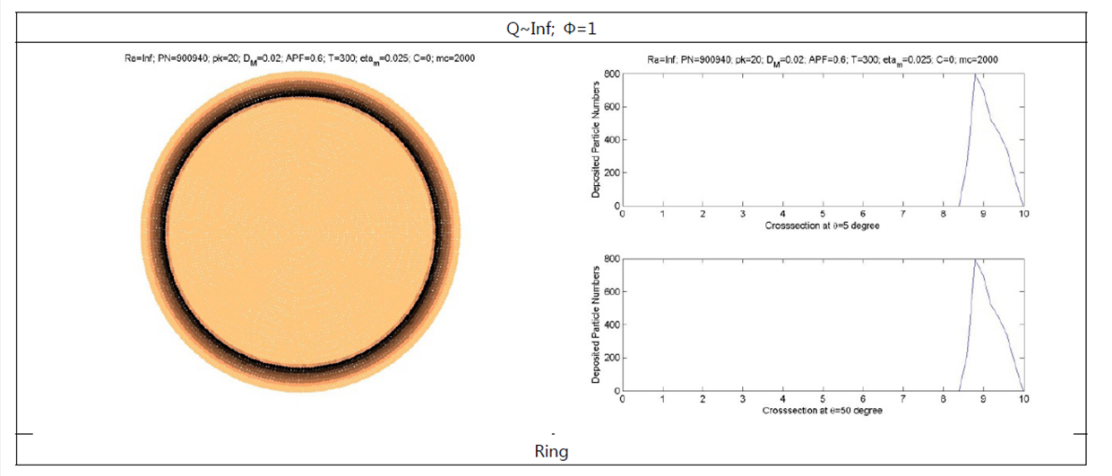

Figure 5.7: The typical ringlike deposit shape at $\Phi = 1$.

in Fig. 5.7. We assume the diffusion-limited evaporation J_d and the corresponding hydrodynamic potential f_i that are computed in Sec. 4.4. The cross-sectional shape in Fig. 5.7 is triangular showing the slope difference inside and outside of the ring deposit. The effects of Φ on ringlike patterns is shown in Fig. 5.8. The mean width of the deposits are increasing with Φ without changing the ringlike nature of patterns.

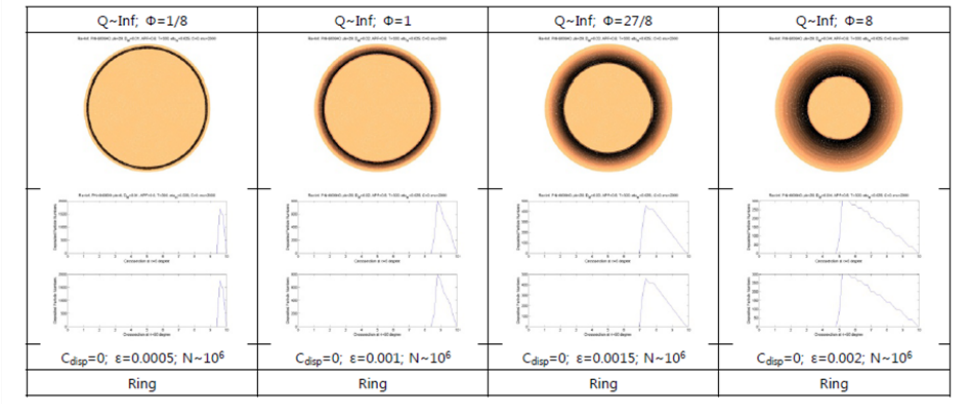

Figure 5.8: The effect of Φ on ringlike patterns.

As Q decreases for fixed Φ, patterns stay ringlike until the value of Q becomes small enough to create wavy shapes. Figure 5.9 shows a time evolution

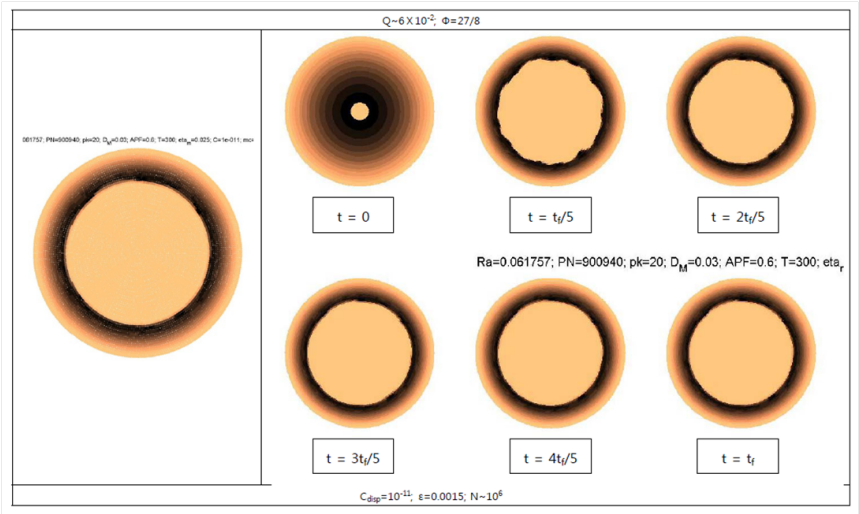

Figure 5.9: Time evolution of a ring formation under a weak interaction.

of a ring shape. The final drying time t_f is divided into six segments and the corresponding shapes are shown on the right side of the figure. A wavy shape appears at $t = t_f/5$ and then disappears as the convective flow becomes stronger with increasing time. The final deposit shape is ringlike.

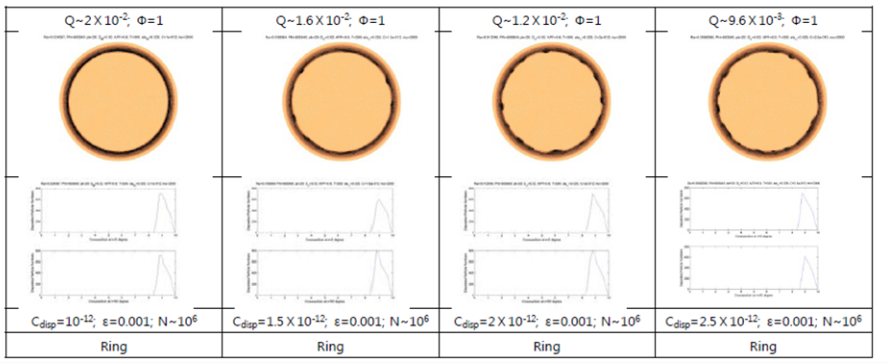

Figure 5.10: Emergence of wavelike patterns by varying Q with Φ fixed.

To further investigate when the wavyness remains on the deposit shape, we change Q from $Q \approx 2 \times 10^{-2}$ to $\approx 9.6 \times 10^{-3}$ at $\Phi = 1$. The final deposit shapes and the corresponding time evolution of each are presented in Fig. 5.10 and in Fig. 5.11, respectively. At time $t = t_f/5$, wavy shapes appear. The

wave number increases and the wavyness persists until the final time. When $Q \approx 9.6 \times 10^{-3}$, three islands are left at $t = t_f/5$ but soon coalesce so that the final pattern is wavy. Later we will see that when Q is small enough (strong interactions), similar islands at earlier times do not easily coalesce and instead persist to the final time.

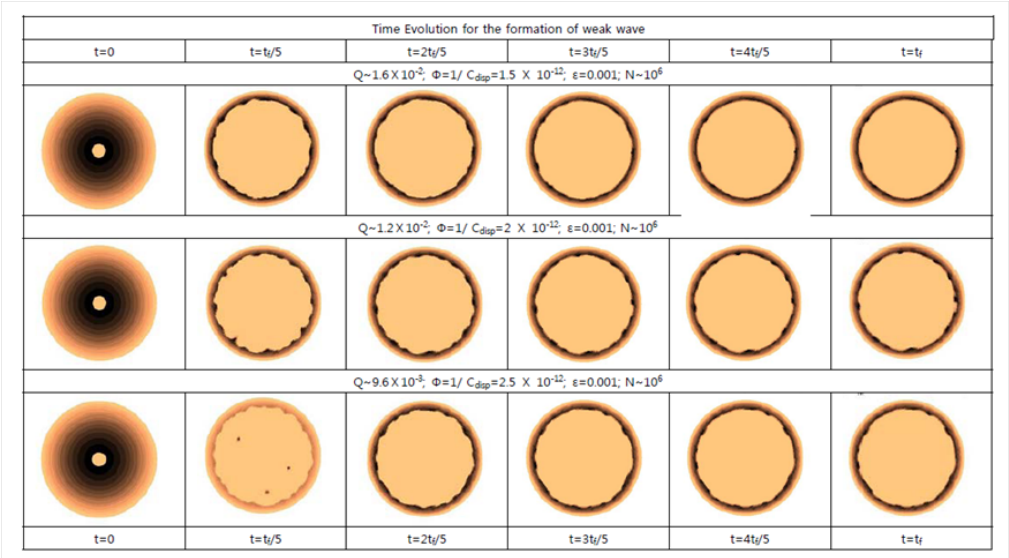

Figure 5.11: Time evolution for the formation of weak wavelike patterns.

5.2.2 Wavelike Instability Patterns

In the previous section we found that wavelike patterns emerge from ringlike ones as Q decreases from ∞ to about 10^{-3} at $\Phi = 1$. At $Q \approx 10^{-3}$ and $\Phi = 1$, the convective flow force and the interaction force are roughly balanced with each other making wavy shapes. Figure 5.12 shows patterns generated with the values of Q close to 10^{-3}. It is noted that the mean thickness increases as Q decreases. Li et al. argued that the characteristic wave lengths of patterns depend only on the mean width of patterns (for example, $\lambda_m = 4.6w$ for pentanol solution) [5]. We find that the mean width can be adjusted by

varying the interaction strength as well as the size or number of particles. Patterns created in the current study shows the proportional relation between wavelengths and mean widths, which agrees with the results by Li et al. (See Figures 5.12 and 5.13).

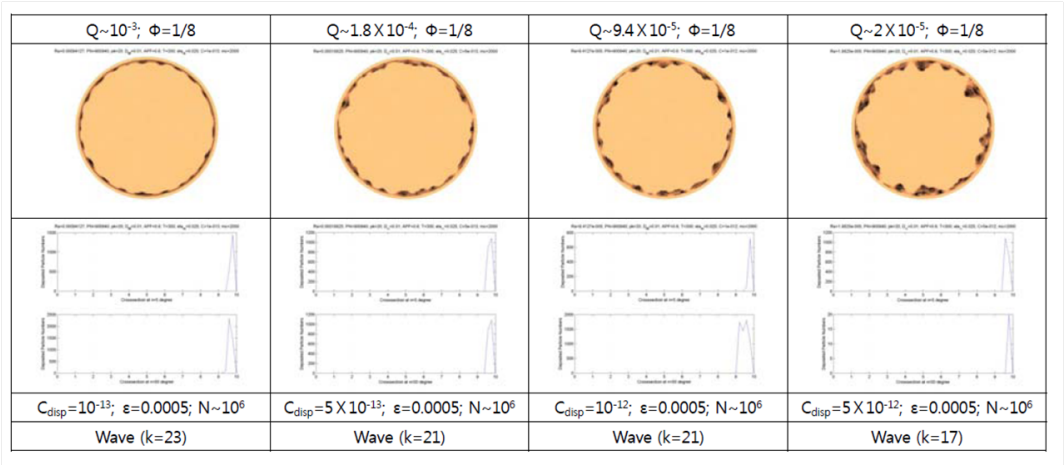

Figure 5.12: The representative behaviors of deposit patterns with the small change near $Q = 10^{-3}$ to show the delicate change of patterns. The value of Q changes from from 10^{-3} to 2×10^{-5} at $\Phi = 1/8$.

Figure 5.13 shows wavelike patterns by changing the value of Φ, while Q is fixed at 10^{-3}. This can be achieved for example by changing the particle number N. The mean width increases with increasing of Φ and the associated wave numbers are decreasing, except when $\Phi = 1/8$. In this case, most of the particles are deposited at a single layer due to the small number of particles, making it hard to clearly identify wave shapes.

The time evolution of wave shapes are shown in Fig. 5.14. At the earlier times in the time series, islands are left behind in the middle because the interaction force is larger than the convective flow force at this stage. However, particles in the islands are eventually transferred to the contact line and join the wavy shapes when convective flows become strong at the later times. Note

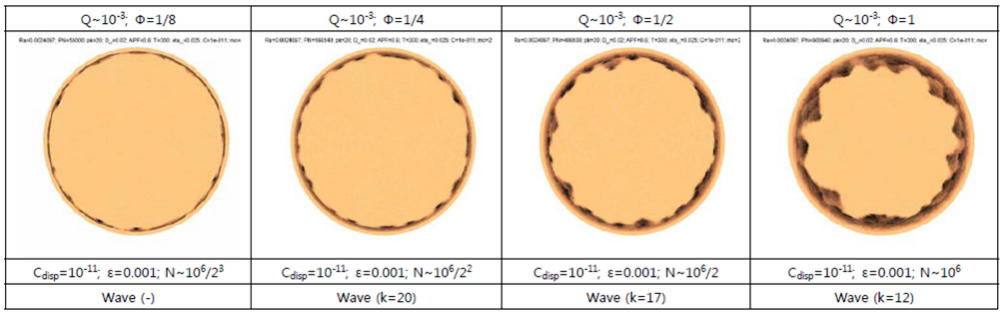

Figure 5.13: Particle number effect on the typical wavelike deposits at $Q = 10^{-3}$.

that the convective flow velocity diverges at the final time as well as at the contact line, making the convective flow potential relatively strong at the final time. At fixed Q, patterns depend strongly on Φ which is clearly shown in the intermediate figures. For example, at the time step $t = 2t_f/t$ and $Q = 10^{-3}$, particles remain in the middle as islands at $\Phi = 1$ while all particles are carried to the contact line with the flow at $\Phi = 1/4$. Since islandlike shapes are formed when the interaction force is stronger than the convective flow force, we again see that the interaction at $\Phi = 1$ is stronger than at $\Phi = 1/4$ with fixed Q.

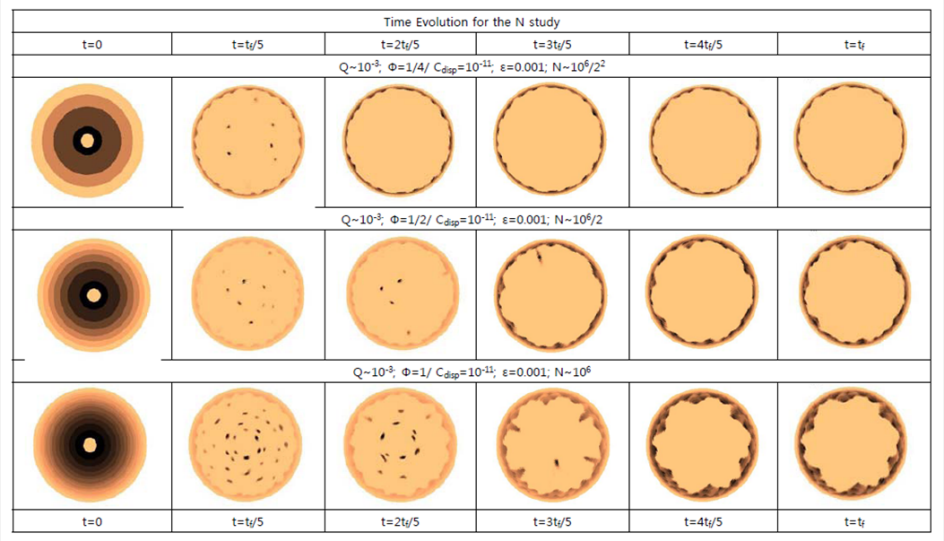

Figure 5.14: Time evolution for the formation of waves at $\epsilon = 0.001$.

Among the wavelike patterns presented in Fig. 5.13 (or 5.14), two different modes are recognized. One mode is as in the second panel in Fig. 5.13 (or in the first row in Fig. 5.14), i.e. a smooth regular scalloped wave pattern. The other mode is as in the fourth panel in the same figure (or in the third row in Fig. 5.14), shows multiple layers of scallops. That is, the undulated surface is not completely smooth. In the third rows of patterns in Fig. 5.14, particles remain in the middle untill $t = 3t_f/5$ and then transfer to the contact line making a second layer of wavelike deposit. Since those particles impinge on the first layer of waves, the mean thickness increases.

5.2.3 Fingerlike Patterns

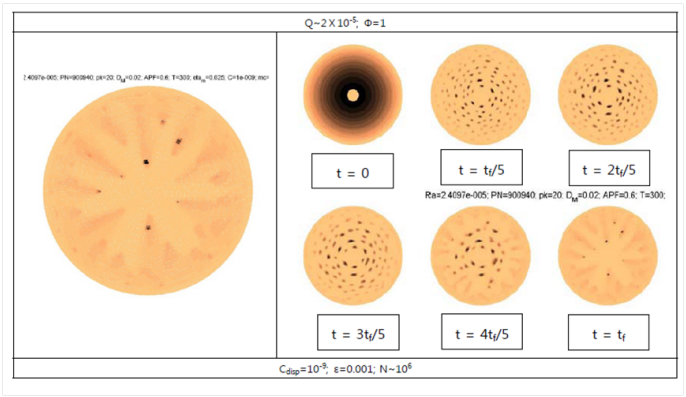

Figure 5.15: A typical fingerlike deposit shape at $Q = 2 \times 10^{-5}$ and $\Phi = 1$

In the previous subsections, we have seen ringlike patterns as $Q \to \infty$ and wavelike patterns at smaller Q and various values of Φ. As Q decreases further, fingerlike patterns emerge. Figure 5.15 shows a typical fingerlike pattern and its time evolution. Since the interaction force is weak compared to the convective flow, island particles are transferred to the contact line making fingerlike traces. Unlike wavelike patterns, fingers are left in the middle because

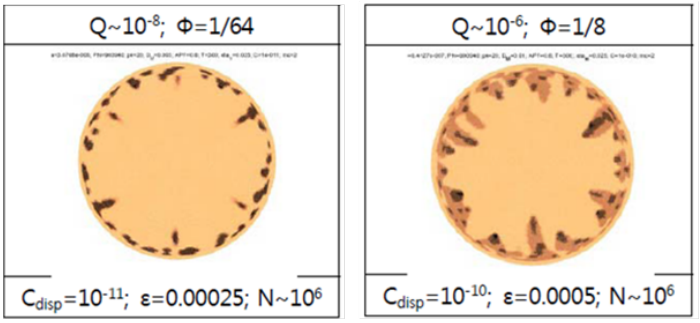

Figure 5.16: Fingerlike patterns near the contact lines.

of the insufficient strength of a convective flow.

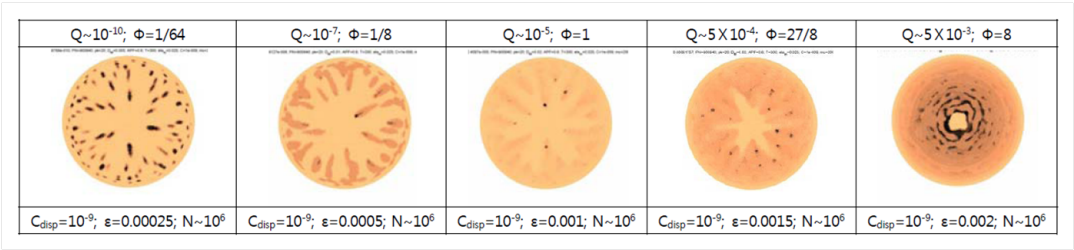

(a) At $C_{disp} = 10^{-9} eV \cdot \mu m^6$.

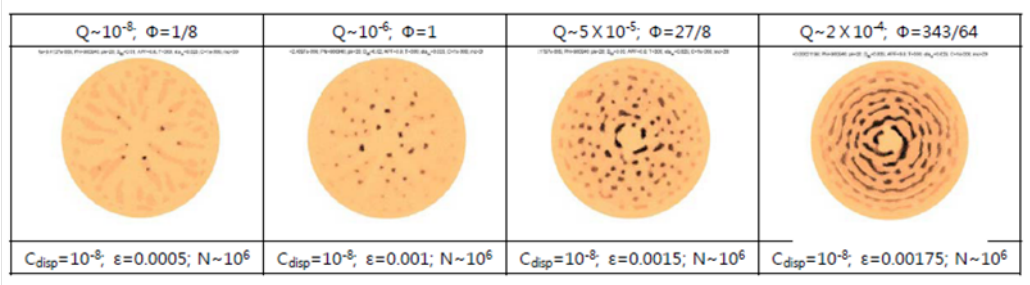

(b) At $C_{disp} = 10^{-8} eV \cdot \mu m^6$.

Figure 5.17: Fingerlike patterns with several particle sizes.

Figures 5.16 and 5.17 depicts fingerlike patterns with various values of Q and Φ. In each figure, Q and Φ both vary with increasing particle size and fixed strength of interaction. Patterns in Fig. 5.16 resemble wavelike patterns near the contact line. Patterns in Fig. 5.17 present wide variations with several different particle sizes. The strength of interaction is $C_{disp} \approx 10^{-9}$ and $10^{-8} eV \cdot \mu m^6$ in Fig. 5.17(b). Isolated fingers in the first and the

second panels of Fig. 5.17(a) transform into connected flowerlike shapes with increased particle sizes. Some of islands remain after evaporation. Fig. 5.17(b) with increased C_{disp}, more islands are left in the middle and particles are uniformly spread around these islands due to the strengthened convective flow with particle sizes.

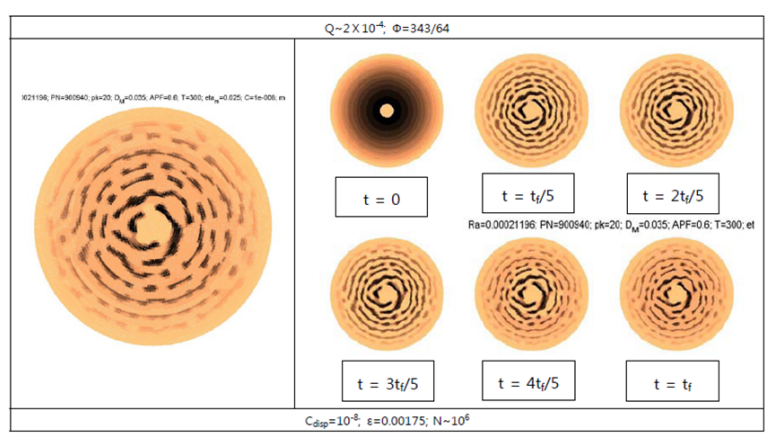

Figure 5.18: Time evolution of a pattern at $Q = 2 \times 10^{-4}$ and $\Phi = 343/64$.

The time evolution presented in Fig. 5.18 shows two features. At the earlier time $t = t_f/5$, the islands stay disconnected except near the contact line whereas at the later time they become connected as particles spread around the island. This is because the convective flow is stronger at later time composed to earlier times, and are also stronger near the contact line.

If the interaction increase further, one finds isolated islands. This case is discussed in the next subsection. The fingerlike patterns are transition patterns between wavelike and islandlike patterns as Q gradually decreases with Φ fixed.

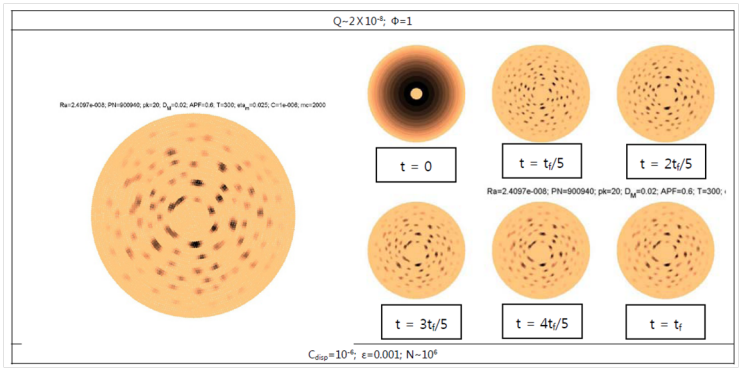

Figure 5.19: The typical islandlike deposit shape when $\epsilon = 0.001$.

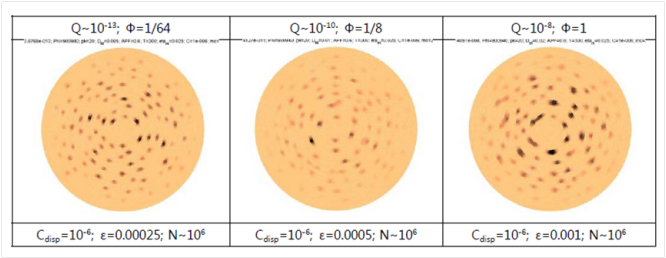

(a) The value of ϵ ranges from $\epsilon = 0.0005$ to $\epsilon = 0.002$.

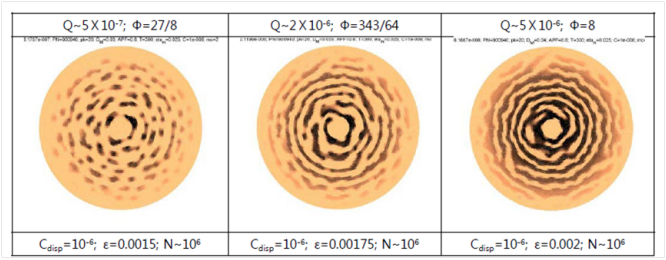

(b) The value of ϵ ranges from $\epsilon = 0.003$ to $\epsilon = 0.004$.

Figure 5.20: Particle size effect on islandlike patterns

5.2.4 Islandlike Patterns

Earlier we found that when interactions between particles vanish, deposit patterns are governed by convective flows and become rings. The other extreme will be when interactions are dominant over convective flows. In this case, the corresponding patterns are islands. Figure 5.19 shows a typical isolated islandlike patterns. Each island has a definite size corresponding to the num-

ber of particles initially distributed on the lattice. On the right side, the time evolution illustrates that islands are formed at the initial time and then remain almost the same except for two or three islands that merge with time.

Islandlike patterns depend on Φ as follows. We find isolated islands at small Φ in Fig. 5.20(a) and connected ones at large Φ in Fig. 5.20(b).

5.3 Pattern Summary

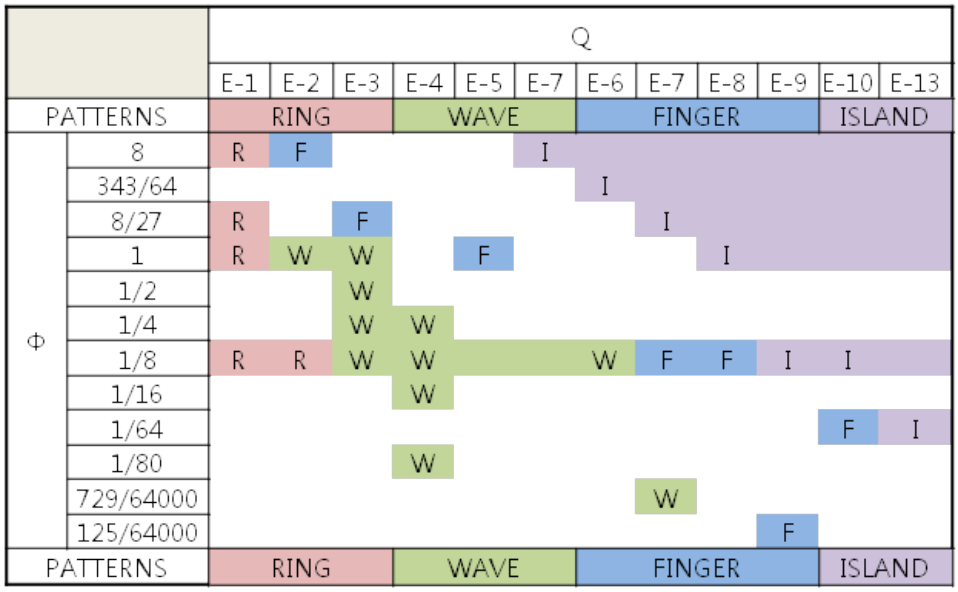

Figure 5.21: A summary table of patterns presented in this chapter.

We summarize all patterns in Fig. 5.21. The rows in the table cover several orders of Q from 10^{-1} to 10^{-13} while the columns show Φ values ranging from 125/64000 ($\approx 2 \times 10^{-3}$) to 8. The morphologies ringlike, wavelike, fingerlike, and islandlike shapes are denoted by different colors and placed in the table according to Q and Φ values. Recall that the dimensionless parameter Q is the ratio of a convective flow potential to an interparticle interaction and

the dimensionless parameter Q is the relative volume fraction of particles. Islandlike patterns are created as Q becomes small while ringlike patterns are generated as Q becomes large. The effect of Φ is clear in this table. As Φ increases, islandlike patterns emerge at relatively large Q meaning that the effectiveness of interaction increases with Φ in the pattern forming process.

Chapter 6

Conclusion

We have examined the deposit pattern formation of an evaporating droplet containing solute particles. As the droplet evaporates, the particles are accumulated near at the pinned contact line due to the asymmetric convective flow and aggregate forming various structures, ranging from simple rings to islandlike patterns. We proposed and successfully demonstrated that wavelike patterns are created because of an inter-particle attraction competing with the convective flow.

We investigated the morphological transformation of the patterns according to the dimensionless numbers Q and Φ. The number Q is a ratio between the convective flow potential and the inter-particle interaction and the number Φ is a relative volume fraction of particles. In the study, the parameter Q is expressed as a function of ϵ and C_{disp}. Physically, ϵ and C_{disp} are determined by the size and surface chemistry of particles, respectively. The value C_{disp} is a constant to determine the strength of interparticle interaction and is related to the surface chemistry of particles. On the other hand, Φ can be varied by the number or the size of particles. If the Q is decreased (i.e., interaction

is strengthened and a convective flow is weakened), wavelike patterns emerge from ring-like ones. In the later stage of the wave formation, some of the pre-formed scalloped (or undulated) waves smooth out, resulting in smaller wave numbers compared to those in the earlier stage. This is because the convective flow increases toward the final drying time. If Q is sufficiently small (i.e., the interaction is sufficiently large), then the inter-particle attraction drives the particles into isolated island-like patterns. In case of the higher Φ, the particles tend to cluster more easily into an island-like pattern because the average inter-particle distance becomes shorter and makes the interaction forces stronger.

It is observed that the stronger the inter-particle interaction C_{disp}, the wider the mean width of the wave patterns. The particles that arrived at the contact line in the later stages of evaporation have insufficient time to fully engage in the patterns before the final drying time. If Φ increases, so does the mean width of the wave patterns. The pattern remains qualitatively the same for different physcial values (the size and the number of particles and the strength of interaction), as long as the two dimensionless parameters Φ and Q are fixed.

Between the wave-like and island-like patterns, transitory finger-like patterns emerge. Finger-like patterns emerge when the interactions are too weak to hold the particles in an island-like shape in the later stages of evaporation. The particles which are parts of the islands at the earlier time are swept away by the strengthened convective flow near the final drying time. They leave traces of finger-like patterns in the middle because there is not enough time for them to reach the contact line. If Φ is large, then particles that are initially part of islands are simply spread around each island due to the strong convective flow.

As noted in Chapter 1, prior work on the self-assembly of interacting nanoparticles deal with diffusion of nano particles in the process. They have not emphasized convective hydrodynamic flows of evaporating solvent. In contrast, the present work considers convection of the solvent induced by evaporation and pattern forming process due to the convection. The Hamiltonian of our coarse lattice model allows to account for both the convection of the solvent and the interaction of the solute at the same time.

We note that there are a number of phenomena ignored in our model that may be important in various experimental settings. These include transfer-limited evaporation (as opposed to diffusion-limited evaporation considered in the current work), Marangoni effects due to surface tension gradient during evaporation, and rheological effects that occur as the particle concentration increases to diverge and slow down the fluid flow near the final drying time.

The diffusion limited evaporation justifies the assumption of quasi-steady processes in the present work. Studies of transfer-limited evaporation is quite rare. The experiments conducted by Deegan and his coworkers found that the transfer-limited evaporation of a droplet leaves ring deposits which are wider than those from diffusion -limited evaporation. On the simulation side, the full hydrodynamic diffusion-convection equation describes transfer-limited evaporation and some important deposit phenomena including coffee ring stains [20]. The main issue in simulation is that quasi-steady processes may not occur in the case of transfer-limited evaporation. The simple coarse grained lattice model developed in the current work may provide a simple but quantitatively accurate measure of the width of ring deposits without considering the full hydrodyanmic equations for transfer-limited evaporation.

Marangoni effects induce a recirculatory flow driven by surface tension gra-

dients produced by latent heat of evaporation. The ratio of substrate thermal conductivity to solvent thermal conductivity determines the direction of the Marangoni flows. These flows can reverse a capillary convective flow toward the contact line and makes deposit patterns at the center rather than at the contact line. For example, fluorescent poly(methyl methacrylate) (PMMA) particles in a drying octane droplet prefers to stay and deposit near the center of the droplet rather than near the contact line because of the Marangoni effect [3]. Accounting for Marangoni effects in our model would require an additional potential term in the Hamiltonian defined in Chapter 4.

In the current model, the droplet dynamics are independent of the dynamics of the particles in that the convective potential is given as known prior to the particle redistribution process. Rheological effects influence the fluid flow, as the viscosity increases with the particle concentration. There are two time regimes in the growth of the rings at the contact line [7]. The ring grows according to a power low at early times, whereas it rapidly grows and diverges at late times. At this late time regime, the hydrodynamic flow and the dynamics of particles are coupled. Our model can account for the coupling by allowing liquid viscosity that determines a convective flow potential to depend on the particle volume fraction.

Bibliography

[1] Zhiqun Lin (editor), Evaporative Self-Assembly of Ordered Complex Structures, *World Science*, **2012**, Printed in Singapore.

[2] D. Kaya, V. A. Belyi, and M. Muthukumara, Pattern formation in drying droplets of polyelectrolyte and salt, *J. Chem. Phys.*, **2010**, 133, 114905.

[3] Hua Hu, and Ronald G Larson, Marangoni Effect Coffee-Ring Depositions, *J. Phys. Chem. B*, **2006**, 110, 7090-7094.

[4] George M. Whitesides and Bartosz Grzybowski, Self-Assembly at All Scales, *Science*, **2002**, 295, 2418-2421.

[5] Fang-I Li, Sean M. Thaler, Perry H. Leo, and John A. Barnard, Dendrimer pattern formation in evaporating drops, *J. Phys. Chem. B*, **2006**, 110, 25838-25843.

[6] Fang-I Li, Perry H. Leo, and John A. Barnard, Dendrimer pattern formation in evaporating drops: solvent, size, and concentration effects, *J. Phys. Chem. B*, **2008**, 112, 14266-14273.

[7] Robert D. Deegan, Olgica Bakajin, Todd F. Dupont, Greb Huber, Sidney R. Nagel, and Thomas A. Witten, Capillary flow as the cause of ring stains fromdried liquid drops, *Nature*, **1997**, 389, 827.

[8] Robert D. Deegan, Olgica Bakajin, Todd F. Dupont, Greg Huber, Sidney R. Nagel, and Thomas A. Witten, Contact line deposits in an evaporating drop, *Physical Review E*, **2000**, 62, 756.

[9] Eran Rabani, David R. Relchman, Philip L. Gelssler, and Louis E. Brus, Drying-mediated Self-assembly of Nanoparticles, *Nature*, **2003**, 426, 271-274.

[10] I. Vancea and U. Thiele, Front Instabilities in Evaporatively Dewetting Nanofluids, *Physical Review E*, **2008**, 78, 041601.

[11] Guy Yosef and Eran Rabani, Self-Assembly of Nanoparticles into Rings: A Lattice-Gas Model, *J. Phys. Chem. B*, **2006**, 110, 20965-20972.

[12] Claudia G. Sztrum, Oded Hod, and Eran Rabani, Self-Assembly of Nanoparticles in Three-Dimensions: Formation of Stalagmites, *J. Phys. Chem. B*, **2005**, Vol 109, 6741-6747.

[13] Guy Orly Kletenik-Edelman, Elina Ploshnik, Asaf Salant, Roy Shenhar, Uri Banin, and Eran Rabani, Drying-Mediated Hierarchical Self-Assembly of Nanoparticles: A Dynamical Coarse-Grained Approach, *J. Phys. Chem. C*, **2008**, 112, 4498-4506.

[14] Oded Hod and Eran Rabani, A coarse-grained model for a nanometer-scale molecular pump, *PNAS*, **2003**, Vol 100, no. 25, 14661-14665.

[15] Claudia G. Sztrum-Vartash and Eran Rabani, Lattice Gas Model for the Drying-Mediated Self-Assembly of Nanorods, *J. Phys. Chem. C*, **2010**, Vol 114, 11040-11049.

[16] J.F. Joanny and P. G. de Gennes, A model for contact angle hysteresis, *J. Chem. Phys.*, **1984**, 81(1), 552-562.

[17] M. Maillard, L. Motte, A. T. Ngo, and M. P. Pileni, Rings and Hexagons Made of Nanocrystals: A Marangoni Effect, *J. Phys. Chem. B*, **2000**, 104, 11871-11877.

[18] Pierre-Gilles de Gennes, Francoise Brochard-Wyart, and David Quere, Capillarity and Wetting Phenomena: Drops, Bubbles, Pearls, Waves, *Springer*, **2004**.

[19] Ken Sekimoto, Ryuichiro Oguma, and Kyozi Kawasaki, Morphological stability analysis of partial wetting, *Ann. Phys*, **1987**, 176.

[20] Kara L. Maki and Satish Kumar, Fast evaporation of spreading droplets of colloidal suspensions, *Langmuir*, **2011**, 27, 11347-11363.

[21] ERIC SULTAN, AREZKI BOUDAOUD and MARTINE BEN AMAR, Size-discriminative self-assembly of nanospheres in evaporating drops, *J. of Engineering Mathematics*, **2004**, 0, 1-15.

[22] A. Vrij, Possible Mechanism for the Spontaneous Rupture of Thin, Free Liquid Films, *Discuss. Faraday Soc.*, **1966**, 42, 23-33.

[23] A. Vrij and J. Th. G. Overbeek, Rupture of Thin Liquid Films Due to Spontaneous Fluctuations in Thickness, *Journal of the American Chemical Society*, **1968**, 90:12, 3074-3078.

[24] R. Xie, A. Karim, J. F. Douglas, C. C. Han, and R. A. Weiss, Spinodal Dewetting of Thin Polymer Films, *Physical Review letters*, **1998**, Vol 81, 6, 1251-31254.

[25] Andrei P. Sommer, Matti Ben-Moshe, and Shlomo Magdassi, Size-discriminative self-assembly of nanospheres in evaporating drops, *J. Phys. Chem. B*, **2004**, 108, 8-10.

[26] Mark A. Ratner, Daniel Ratner, Nanotechnology, *Prentice Hall*, 1 edition, **2002**, November 18.

[27] L. Motte, E. Lacaze, M. Maillard, and M. P. Pileni, Self-Assemblies of Silver Sulfide Nanocrystals on Various Substrates, *Langmuir*, **2000**, 16, 3803-3812.

[28] Orly Kletenik-Edelman, Elina Ploshnik, Asaf Salant, Roy Shenhar, Uri Banin and, Eran Rabani, Drying-Mediated Hierarchical Self-Assembly of Nanoparticles: A Dynamical Coarse-Grained Approach, *J. Phys. Chem. C*, **2008**, Vol 112, 4498-4506.

[29] Sung-Hwan Choi and Bi-min Zhang Newbya, Dynamic contact angle in rim instability of dewetting holes, *J. Chem. Phys.* , **2006**, 124, 054702-1.

[30] Yuji Asano, Akitaka Hoshino, Hideki Miuaji, Yoshihisa Miyamoto and Koji Fukao, Pattern formation by rim instability in dewetting polymer thin films, *Nonlinear Dynamics in Polymeric Systems*, **Chapter15**.

[31] F. Brochard-Wyart, and C. Redon, Dynamics of liquid rim instabilities, *Langmuir*, **1992**, 2324-2329.

[32] Jacob N. Israelachvili, Intermolecular and Surface Forces, *Academic Press*, **2011**.

[33] Xiaoying Shen, Chih-Ming Ho, and Tak-Sing Wong, Minimal Size of Coffee Ring Structure, Shen, Ho, and Wong, *J. Phys. Chem. B*, **2010**, 114, 5269-5274.

[34] Fengting T. Xu, Sean M. Thaler, and John A. Barnard, Structural and mechanical properties of dendrimer-mediated thin films, *J. Vac. Sci. Technol. A 23(4)*, Jul/Aug **2005**, 1234-1237.